THE COSMIC-RAY ISOTOPE SPECTROMETER FOR THE ADVANCED COMPOSITION EXPLORER

E. C. STONE, C. M. S. COHEN, W. R. COOK, A. C. CUMMINGS, B. GAULD, B. KECMAN, R. A. LESKE, R. A. MEWALDT and M. R. THAYER
California Institute of Technology, Pasadena, CA 91125, U.S.A.

B. L. DOUGHERTY*, R. L. GRUMM, B. D. MILLIKEN†, R. G. RADOCINSKI and M. E. WIEDENBECK
Jet Propulsion Laboratory, Pasadena, CA 91109, U.S.A.

E. R. CHRISTIAN, S. SHUMAN, H. TREXEL and T. T. VON ROSENVINGE
NASA/Goddard Space Flight Center, Greenbelt, MD 20771, U.S.A.

W. R. BINNS, D. J. CRARY‡, P. DOWKONTT, J. EPSTEIN, P. L. HINK, J. KLARMANN, M. LIJOWSKI and M. A. OLEVITCH
Washington University, St. Louis, MO 63130, U.S.A.

Abstract. The Cosmic-Ray Isotope Spectrometer is designed to cover the highest decade of the Advanced Composition Explorer's energy interval, from ∼50 to ∼500 MeV nucl^{-1}, with isotopic resolution for elements from $Z \simeq 2$ to $Z \simeq 30$. The nuclei detected in this energy interval are predominantly cosmic rays originating in our Galaxy. This sample of galactic matter can be used to investigate the nucleosynthesis of the parent material, as well as fractionation, acceleration, and transport processes that these particles undergo in the Galaxy and in the interplanetary medium.

Charge and mass identification with CRIS is based on multiple measurements of dE/dx and total energy in stacks of silicon detectors, and trajectory measurements in a scintillating optical fiber trajectory (SOFT) hodoscope. The instrument has a geometrical factor of ∼r250 cm^2 sr for isotope measurements, and should accumulate $\sim 5 \times 10^6$ stopping heavy nuclei ($Z > 2$) in two years of data collection under solar minimum conditions.

1. Introduction

The Advanced Composition Explorer (ACE) will perform comprehensive studies of the elemental, isotopic, and ionic charge state composition of energetic nuclei from H to Zn ($1 \leq Z \leq 30$) from a vantage point located $\sim 1.5 \times 10^6$ km sunward of Earth, near the L1 libration point. These observations will address a wide range of questions concerning the origin, acceleration and transport of energetic nuclei from solar, interplanetary, and galactic sources. ACE includes six high-resolution

* Present address: Mail Stop 264–33, California Institute of Technology, Pasadena, CA 91125, U.S.A.
† Present address: Lucent Technologies, Naperville, IL 60566, U.S.A.
‡ Present address: Pacific-Sierra Research Corp., Warminster, PA 18947, U.S.A.

Space Science Reviews **96:** 285–356, 1998.

spectrometers and three interplanetary monitoring instruments that together will measure composition at energies ranging from <1 keV nucl^{-1} (characteristic of the solar wind) to $\sim$500 MeV nucl^{-1} (characteristic of galactic cosmic radiation). The Cosmic-Ray Isotope Spectrometer (CRIS), one of these six spectrometers, is designed to measure the elemental and isotopic composition over the energy range from $\sim$50 to $\sim$500 MeV nucl^{-1} with excellent mass resolution and collecting power.

The primary objective of the ACE mission is to determine and compare the elemental and isotopic composition of several distinct samples of matter, including the solar corona, the interplanetary medium, the local interstellar medium, and galactic matter. ACE will study matter from the Sun by measuring solar wind (SW) and solar energetic particles (SEPs). Matter from the local interstellar medium (LISM) will be observed at energies of $\sim$1 keV nucl^{-1} as interstellar neutral particles enter the heliosphere and are ionized to become solar wind 'pickup ions'. Some of these ions are also observable as 'anomalous cosmic rays' (ACRs) once they have been convected out to the solar wind termination shock and accelerated to energies of $\sim$1 to 100 MeV nucl^{-1}. Galactic cosmic rays (GCRs) provide a sample of matter that enters the heliosphere from other regions of the Galaxy.

CRIS is the primary instrument responsible for measuring galactic cosmic-ray composition on ACE. Table I summarizes the essential features of this instrument. The remainder of the paper presents a more detailed discussion of the objectives, the design, and the measured performance of CRIS.

2. Scientific Objectives

Cosmic rays consist of energetic electrons and nuclei which are a direct sample of material from beyond the solar system. The energy density of cosmic rays is comparable to the energy densities of interstellar gas, interstellar magnetic fields, and starlight. Thus the cosmic rays are an important part of our astrophysical surroundings. It is generally believed that supernovae provide the energy carried by cosmic rays, but many details of where and how the cosmic rays are accelerated to high energies remain unknown. Unlike photons, which propagate on straight lines from their sources, cosmic rays are charged and hence spiral around the galactic magnetic field lines. As a consequence, their arrival directions tell us nothing about their sources. Instead, essential clues to the origin and history of cosmic rays may be found in the relative abundances of elements and of isotopes. Cosmic rays consist primarily of hydrogen nuclei ($\sim$90% by number), with helium making up the bulk of the remaining particles. Heavier nuclei only account for $\sim$1%. Nonetheless, most of the available information about cosmic-ray origin comes from the elemental and isotopic composition of the heavier cosmic rays.

CRIS will investigate many of the same processes as the other isotope spectrometers on ACE. The galactic cosmic-ray source (GCRS) composition for the

TABLE I
Summary of CRIS characteristics

Characteristic	Value	Details[a]
Measurement objective	Elemental and isotopic composition of galactic cosmic rays	§2
Measurement technique	Multiple-ΔE vs residual energy plus trajectory	§3.1
Sensor system		
Energy loss measurements	Si(Li) detectors (3 mm thick × 10 cm diameter, some with active guard rings) in 4 stacks of 15 detectors each	§4.2, T5
Trajectory measurements	Scintillating Optical Fiber Trajectory (SOFT) hodoscope, position resolution < 100 μm r.m.s, 7.2 cm lever arm	§4.1
Charge interval		§8.1, F18
Primary interval	$4 \leq Z \leq 28$	
Extended interval	$1 \leq Z \leq 30$	
Energy interval for mass analysis		§8.1, F18
O	60–280 MeV nucl^{-1}	
Si	85–400 MeV nucl^{-1}	
Fe	115–570 MeV nucl^{-1}	
Field of view		F6
Primary FOV [b]	45° half angle	
Full FOV	70° half angle	
Geometrical factor (for $\theta < 45°$)	$\sim$250 cm^2 sr	§8.2, F19
Event yields (solar minimum; $\theta < 45°$)		§8.2, F20
Be	3.0×10^4 yr^{-1}	
O	8.9×10^5 yr^{-1}	
Si	1.7×10^5 yr^{-1}	
Fe	1.4×10^5 yr^{-1}	
Mass resolution (r.m.s.)		§8.3, §9.1, F21, F23, §A
O	$\lesssim$ 0.15 amu	
Fe	$\lesssim$ 0.25 amu	
Resource utilization		§7
Dimensions ($l \times w \times h$)	53.3 cm × 43.8 cm × 23.5 cm	
Mass	29.2 kg	
Instrument power	12 W	
Bit rate	464 bits s^{-1}	

[a]Sections (§), Figures (F), and Tables (T) containing additional details.
[b]The definition of a 'primary' field of view is somewhat arbitrary. In optimizing the instrument design, 45° was treated as a practical maximum angle.

dominant heavy elements bears a remarkable resemblance to the pattern of abundances found in solar system material, although more subtle differences between these populations of matter are of great interest (see Section 2.1). Both cosmic rays and the solar corona/solar wind show evidence of having undergone chemical alteration, and the resulting fractionation patterns are strikingly similar. Furthermore, it is widely thought that diffusive shock acceleration is responsible for energizing galactic cosmic rays, just as it is for accelerating anomalous cosmic rays and for producing energetic particle events in interplanetary space. Thus the physical phenomena addressed by CRIS are in many respects the same as those studied with other ACE spectrometers, but on larger spatial, temporal, and energy scales. The remainder of this section briefly outlines some of the specific measurements CRIS is designed to make.

It has long been recognized that in cosmic rays the observed abundance ratio (Li+Be+B)/(C+N+O) exceeds the value found in solar system material by a factor of about 10^5, and that this must be a measure of how much material cosmic rays have traversed since they were accelerated. Specifically, cosmic rays consist of primary nuclei, that is, nuclei such as C and O which reach Earth without undergoing fragmentation, and secondary nuclei, such as Li, Be, and B, which are the products of fragmentation reactions in the interstellar medium.

Primary cosmic rays must be products of stellar nucleosynthesis, but it is not known what types of stars are primarily responsible for producing this material, or whether the acceleration of the cosmic rays has any direct association with the stellar sources responsible for the nucleosynthesis of the accelerated particles. For example, supernovae explosions may accelerate material from the parent stars, or perhaps supernova shocks accelerate material which was previously ejected into interstellar space by other supernovae explosions and stellar winds. In any case, successful models of how cosmic rays propagate will both account for secondary production and provide information on the spatial distribution of sources. Using such models, it is possible to determine the GCRS abundances and gain information about the nature of the sources themselves (e.g., see Stone and Wiedenbeck, 1979). Hence high-resolution measurements by CRIS of cosmic-ray isotopes will provide vital clues to the astrophysics of our Galaxy.

In addition to stable isotopes, the cosmic rays contain long-lived radioactive nuclides of either primary or secondary origin. Table II lists the decay modes and half lives of the radioactive species with atomic number $Z \leq 30$ that should be observable. The observed abundances of these ‘clock’ isotopes can be used for establishing various time scales related to the origin of cosmic rays.

There are still important gaps in our understanding of the origin of galactic cosmic rays, both in terms of the source of the parent material from which they are derived and in terms of the details of how and where they are accelerated to relativistic energies. Narrowing the range of possible explanations for the origin and propagation history of galactic cosmic rays is the observational goal of CRIS.

TABLE II
Radioactive nuclides

Nuclide	Decay Mode	Partial Half life[a]
^{7}Be	ec	53 days
^{10}Be	β^-	1.5 Myr
^{14}C	β^-	5730 yr
^{26}Al	β^+	0.87 Myr
	ec	4.0 Myr
^{36}Cl	β^-	0.30 Myr
^{37}Ar	ec	35 days
^{41}Ca	ec	0.10 Myr
^{44}Ti	ec	49 yr
^{49}V	ec	330 days
^{51}Cr	ec	28 days
^{53}Mn	ec	3.7 Myr
^{54}Mn	ec	312 days
	β^+	400 Myr
	β^-	0.8 Myr[b]
^{55}Fe	ec	2.7 yr
^{56}Ni	ec	6.1 days
^{56}Ni	β^+	$\gtrsim$ 1 yr
^{57}Co	ec	270 days
^{59}Ni	ec	76000 yr

[a]Laboratory half lives.
[b]Estimated value (Zaerpoor et al., 1997).

There are several distinct groups of isotopes that one can take advantage of to address various aspects of this problem:

– Primary isotopes: these isotopes reveal the conditions of nucleosynthesis in the cosmic-ray sources. Models of cosmic-ray propagation, based in large part on the other isotope groups, are essential for determining the abundances of the primary isotopes. As will be discussed below, the primary isotopes have undergone some type of chemical fractionation. It is of major interest to understand how and where this has occurred.

– Acceleration delay clocks: primary isotopes which decay by electron capture can provide information about the elapsed time between nucleosynthesis and particle acceleration.

– Propagation clocks: secondary isotopes which decay by $\beta^{\pm}$ emission can measure the average time between the production of these particles and their escape from the Galaxy (Ptuskin and Soutoul, 1998).

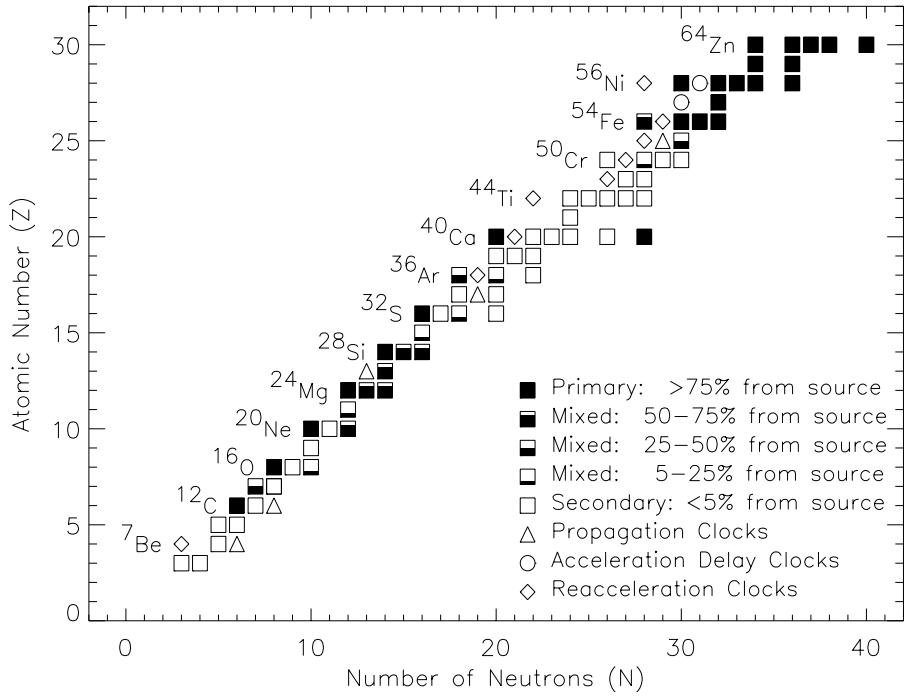

Figure 1. Chart showing the atomic number Z and neutron number N for nuclides present in galactic cosmic rays. The symbols used for the various nuclides indicate the types of studies to which they are expected to contribute, as discussed in the text. In some cases these assignments are uncertain, particularly for the rarer nuclides.

– Reacceleration clocks: secondary isotopes which decay solely by electron capture can do so only if their velocities have, at some time, been much lower than the velocities at which they are observed. Hence they are potentially probes of energy changing processes that occur during propagation in the Galaxy.

Figure 1 shows which isotopes are in these different groups. Examples of each are discussed in the following paragraphs.

2.1. PRIMARY ISOTOPES

Ratios of individual GCRS element abundances to the corresponding solar system elemental abundances are ordered by first ionization potential (FIP): elements with FIP below ∼10 eV are about 5 times more abundant in the galactic cosmic-ray sources than are the higher FIP elements (see Figure 2). A similar FIP effect is well known for solar energetic particles (e.g., Meyer, 1985; Stone, 1989) and is presumably related to the fact that ions, being charged, are transported from the photosphere into the corona more efficiently than neutrals. A model which could perhaps account for the FIP effect in galactic cosmic rays would have the source ejecting its outer envelope for a long period with a FIP selection effect (as the

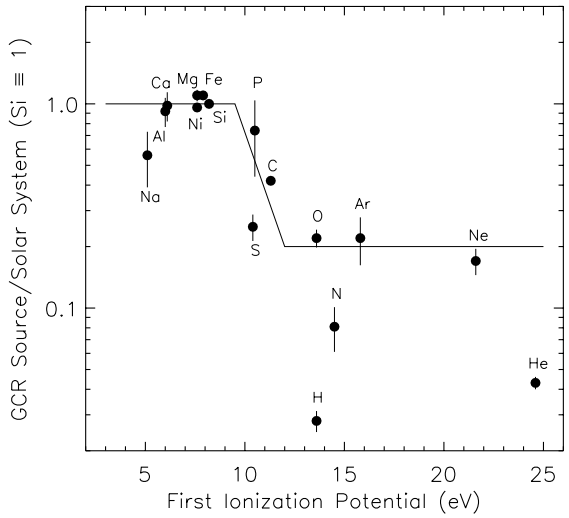

Figure 2. Ratio of galactic cosmic-ray source abundance to solar system abundance versus the element first ionization potential (FIP), normalized to 1 for Si. Cosmic-ray values are from Lund (1989) and are based primarily on data from the HEAO-3-C2 experiment (see Engelmann et al., 1990). More recent data at lower energies from *Ulysses* (DuVernois and Thayer, 1996) are in generally good agreement with these values. The solid line indicates the general trend of the heavy element data. Cosmic-ray hydrogen and helium are distinctly underabundant, even compared to the other high-FIP elements.

sun does) followed by a supernova shock which sweeps up and accelerates this material. Recently it has been claimed (Meyer et al., 1998; Ellison et al., 1998) that the FIP effect is due to non-volatiles being accelerated as grains, while the volatiles are accelerated as individual nuclei (i.e., they propose that the FIP effect is misnamed and really is a volatility effect). In any case, it appears that the cosmic rays have undergone a chemical fractionation process, the origins of which are uncertain.

The GCRS abundances should reveal conditions in the sources themselves. Elemental abundances can probe the chemical processes which fractionate the material prior to acceleration. Such processes should have little, if any, influence on the relative abundances of the isotopes of an element. Particle acceleration, however, is likely to depend on the particle's rigidity, and therefore on its mass-to-charge ratio. Nevertheless, such effects may average out when one observes the composition resulting from a large number of acceleration events, as has been seen in solar energetic particle data (Breneman and Stone, 1985; Stone, 1989). Thus it is thought that the isotopic composition of the GCRS should serve primarily as an indicator of the nuclear processing that the material has undergone.

The abscissa in Figure 3 shows, for different elements, the ratios of low abundance isotopes of each element to the corresponding dominant isotope. The ordinate of Figure 3 shows for each such ratio the GCRS deduced value divided by

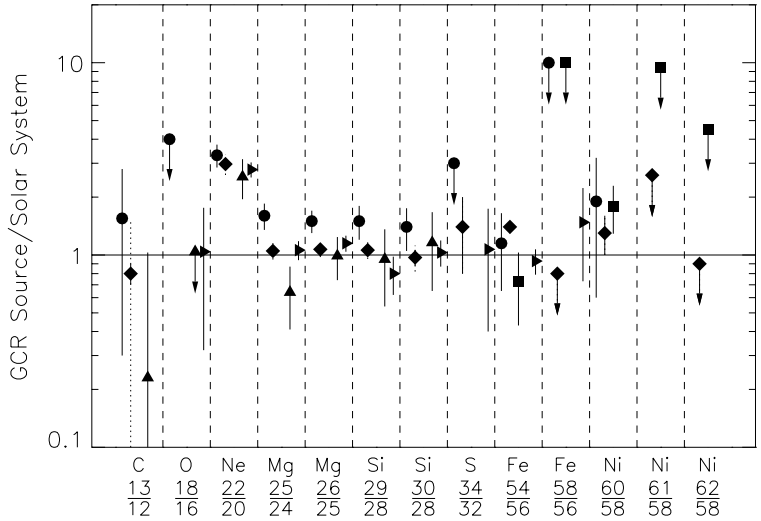

Figure 3. Observed values of various galactic cosmic-ray source isotopic abundance ratios divided by the corresponding solar system ratios. The labels along the abscissa indicate the element and the mass numbers of the isotopes involved in the plotted ratios. Note that in some cases only upper limits are presently available. Symbols: circle – data from prior to 1989, summarized by Mewaldt (1989); diamond – *Ulysses* data from Connell and Simpson (1995, 1997a), Thayer (1997); square – ISEE-3 data from Leske and Wiedenbeck (1993), Leske (1993); triangle pointing up – CRRES data from DuVernois et al. (1996); triangle pointing right – Voyager data from Lukasiak et al. (1997), Webber et al. (1997). The *Ulysses* points are shown with two error bars – the short, solid bars indicate the contribution from the statistical errors in the measurements while the longer, dashed bars give an estimate of the overall uncertainty in the source abundances when propagation errors are also taken into account. For isotopes with large secondary components such as ^{13}C the propagation errors dominate.

the solar system value. With the exception of Ne, most of the ordinate values are very near to unity, i.e., the GCRS isotopic compositions are very similar to those of the solar system. On the other hand, the existing measurements can be greatly improved upon by CRIS and real differences may emerge which are currently obscured by large uncertainties. The Ne anomaly has been known for some time (Fisher et al., 1976). It has been proposed by Cassé and Paul (1982) that Wolf–Rayet stars contribute approximately 2% of all cosmic-ray source material (and $\sim$25% of heavy nuclei), but that the high ^{22}Ne/^{20}Ne ratio ($\sim$120) in the material ejected from Wolf–Rayet stars could account for the ^{22}Ne excess in the GCRS.

2.2. ACCELERATION DELAY CLOCKS

The observed correlation of the fractionation pattern observed in cosmic-ray elemental abundances with atomic properties (Figure 2) suggests that the source material experiences some time at temperature $\lesssim$ 10 eV after nucleosynthesis and before acceleration. If cosmic rays were produced from grains formed in the ejecta of a supernova explosion this time could be relatively short. On the other hand,

if the accelerated material were injected from the coronas of flare stars the time delay could be a significant fraction of the age of the Galaxy. Thus a determination of the time delay between synthesis and acceleration could prove decisive in distinguishing among models for the origin of cosmic rays.

It has been proposed (Soutoul et al., 1978) that this time delay can be established using observations of the abundances of radioactive nuclides which are produced in supernova explosions and can decay only by electron capture. In a low-temperature environment these species will decay, but once they are accelerated they are rapidly stripped of their electrons and become effectively stable. The most promising candidates are ^{59}Ni and ^{57}Co, which have half lives $\sim 10^5$ years and $\sim$1 year, respectively, if they are not stripped of their electrons (see Table II).

There are already indications that there may have been a significant delay ($>10^5$ years) between cosmic-ray nucleosynthesis and acceleration. For example, Connell and Simpson (1995) have reported a ^{59}Ni/^{58}Ni ratio which suggests the absence of ^{59}Ni in the cosmic-ray source. The isotope ^{59}Co, which is produced by the decay of ^{59}Ni, can also serve as an indicator of this decay. Leske (1993) has also reported a significant delay, based on observations of ^{59}Co and an upper limit on ^{59}Ni.

Because the isotopes of mass 57 and 59 have low abundances and, in the cases of ^{59}Ni and ^{57}Fe, are adjacent to nuclides that are much more abundant, measurements with excellent mass resolution and large collecting power are needed to definitively determine whether the cosmic-ray source material has experienced a long time delay prior to acceleration. CRIS is expected to provide measurements of the necessary quality.

2.3. PROPAGATION CLOCKS

Propagation clocks are secondary isotopes which decay by $\beta^{\pm}$ emission. These provide a measure of the cosmic-ray 'confinement time' (or 'escape time'), the average time which passes between the production of cosmic rays and their escape from the Galaxy. A convenient parameter to use in discussing the decay of propagation clocks is the 'surviving fraction', the ratio of the observed abundance to the abundance expected if the nuclei did not have time to decay. This quantity is plotted in Figure 4 as a function of the half life of the nuclide, based on a standard, homogeneous 'leaky-box' model of cosmic-ray propagation.

The confinement time for cosmic rays in the Galaxy has been estimated from the surviving fraction of ^{10}Be, which decays by β^- emission with a half life of 1.5×10^6 years. The result is only about 1–2 $\times$ 10^7 years (Wiedenbeck and Greiner, 1980; Garcia-Muñoz et al., 1977). The corresponding mean gas density in the confinement volume, $\sim$0.3 atoms cm^{-3}, is less than commonly accepted values of the mean interstellar gas density in the galactic disk and it has therefore been argued that cosmic rays must spend a significant amount of time outside of the disk. The short confinement time places heavy requirements on the energy output of the

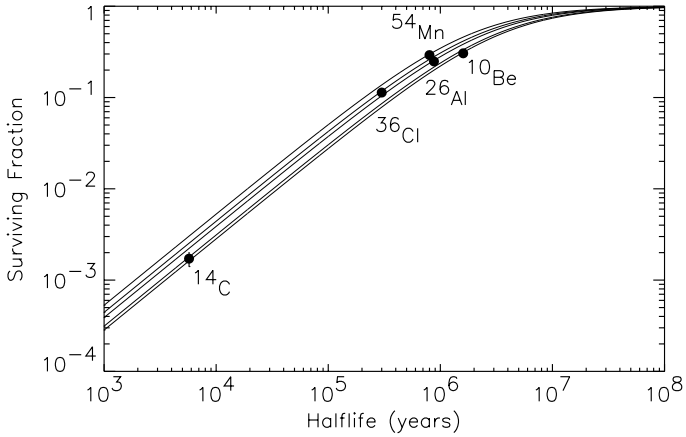

Figure 4. Expected surviving fraction of various radioactive secondary nuclides as a function of their half lives. The calculated surviving fractions are based on a leaky box model of cosmic-ray propagation with the confinement time deduced from the measured ^{10}Be/^{9}Be ratio. The different curves, corresponding to different nuclear masses (plotted for $A = 10$, 14, 26, 36, and 54 from bottom to top), are due to differences in the mean path length for nuclear fragmentation loss for different species. In these calculations time dilation, ionization energy loss, and solar modulation effects were neglected.

sources of cosmic rays ($\sim 10^{41}$ ergs s^{-1} in our Galaxy (Berezinski et al., 1990)) and also means that the GCR source material could be significantly younger than solar system matter.

The isotope ^{10}Be predominantly measures the confinement time for C, N, and O. It is important to study other such clocks to determine whether or not other elements (e.g., those near the iron peak), might have different histories. Possibilities include ^{26}Al, ^{36}Cl, and ^{54}Mn, although the case of ^{54}Mn is difficult because its half life for β^- decay has not been directly measured (Zaerpoor et al., 1997).

Recently, *Ulysses* observations of 92 ^{26}Al nuclei have yielded a confinement time of 16 ± 3 million years (Connell and Simpson, 1997b). CRIS is expected to observe about 3000 ^{10}Be, 3000 ^{26}Al, and 1000 ^{36}Cl in two years (see Section 8.2). With measurements having good statistical accuracy for several clock isotopes over a range of half lives it may also be possible to test more realistic models of cosmic-ray propagation (Ptuskin and Soutoul, 1998), since such data will provide some sensitivity to the distribution of confinement times in the Galaxy, in addition to providing the mean of this distribution.

The isotope ^{14}C is another potentially interesting secondary which decays by β^- emission. Its half life is very short in comparison with the other clock isotopes discussed above, only 5730 years. Secondary ^{14}C produced by fragmentation of heavier nuclei in the interstellar medium will be observable only if it is produced in the immediate neighborhood of the solar system. Based on a homogeneous leaky-box model of cosmic-ray propagation with the confinement time deduced from the ^{10}Be abundance, one expects a ^{14}C surviving fraction of ~ 1–2×10^{-3}

(see Figure 4). With the CRIS instrument's large geometrical factor it should be possible to observe ∼30 ^{14}C nuclei in 2 years under these conditions. However, if the interstellar density in the region sampled during the 5730 yr half life of ^{14}C were significantly lower or higher than the average density in the confinement volume, the number of ^{14}C nuclei produced in this local volume would be correspondingly modified. By comparing the density deduced from the ^{14}C measurement with astronomical measurements of the density distribution in the local interstellar medium, it may be possible to derive a limit on the cosmic-ray diffusion coefficient in the local interstellar medium, since this parameter affects the size of the region sampled by the ^{14}C clock.

2.4. REACCELERATION CLOCKS

The abundances of nuclides that can decay only by electron capture are sensitive to the density of the medium in which the particles propagate and to the particle energy at which the propagation occurs. At high energies, cosmic rays spend essentially all their time fully stripped of their orbital electrons, so the electron capture mode of decay is no longer possible and these particles are effectively stable. At somewhat lower energies, ∼100 MeV nucl^{-1} and below, the particles will occasionally attach an electron from the surrounding medium and retain it until the electron is either stripped back off in a collision with an atom in the interstellar gas or until the nucleus captures it and decays. In a high-density medium, the time between stripping collisions is short and the nuclei attain an equilibrium charge-state distribution with decay losses depending on the fraction of this distribution which is not fully stripped and on the electron capture half life. At low densities, nuclei which attach an electron are likely to decay before it can be stripped off, so the decay rate for these particles depends primarily on their electron attachment cross section. Thus abundances of electron capture nuclei can, in principle, provide information about the interstellar density in the propagation medium (see, for example, Letaw et al., 1993, and references therein) which can complement that obtained from the propagation clocks discussed above.

The cross sections for electron stripping and, particularly, for electron attachment are very strong functions of the velocity of the nucleus. If, for example, the electron capture nuclide ^{55}Fe ($T_{1/2} = 2.6$ yr in the laboratory) is produced by fragmentation of ^{56}Fe at 500 MeV nucl^{-1} and propagates at essentially this same energy for $\sim 10^7$ years, there is negligible chance that it will decay. However, if the ^{55}Fe is produced at 50 MeV nucl^{-1} and propagates at this low energy until reaccelerated by an interstellar shock, there is a significant chance that it will decay before the reacceleration. It has been proposed (Letaw et al., 1985) that electron capture nuclides can be used to probe changes in cosmic-ray energies during propagation.

A variety of secondary isotopes that can decay only by electron capture are available for such investigations. These are listed in Table II, along with their laboratory half lives. (With only a single electron attached half lives are a factor

$\sim$2 longer.) The interpretation of the abundances of electron capture secondaries will be complicated by the joint dependence on density and particle energy, and also by the energy changes that occur due to solar modulation as the particles enter the heliosphere. With precise measurements of the abundances of a range of electron capture nuclides it may be possible, for the first time, to extract some of the information carried by this class of cosmic rays.

3. Design Requirements and Instrumental Approach

If CRIS is to meet the objectives discussed in Section 2 and make a significant contribution beyond previous experiments, it must be capable of precisely measuring even the rarest cosmic-ray nuclei between Be ($Z = 4$) and Ni ($Z = 28$). The separation of rare nuclides from adjacent abundant species (for example, ^{57}Fe from ^{56}Fe) demands a mass resolution $\lesssim$0.25 amu. In addition, the measurement of rare isotopes demands sufficient collecting power to accumulate a statistically significant sample of these particles over the duration of the ACE mission. The necessary geometrical factor, $\gtrsim$ 100 cm^2 sr (see Section 8.2), is considerably larger than that of previous cosmic-ray isotope spectrometers flown in space.

The sensor approach that was adopted for CRIS, using multiple measurements of dE/dx vs total energy (see Section 3.1), has been developed and proven over the course of a large number of space missions. During the ACE Definition Study a critical evaluation was made of instrumental requirements for achieving the needed 0.25 amu mass resolution. This process was greatly aided by the heritage of analyses and accelerator data accumulated from earlier isotope spectrometers, such as those flown on ISEE-3, CRRES, *Ulysses*, SAMPEX, and WIND. The joint requirements for precise mass determination and large collecting power influenced essentially all aspects of the CRIS instrument design, placing requirements on the sensors, the electronics, and the mechanical construction. They also necessitated an extensive program of accelerator tests and calibrations, both of individual sensor elements and of the completed instrument.

3.1. Mass and Charge Analysis Technique

In CRIS, the charge and mass of detected particles are identified based on the energies they deposit in coming to rest in a stack of silicon solid-state detectors. When a particle of charge Z, mass M, and kinetic energy E penetrates an amount of matter L and emerges with residual kinetic energy E', the change in its range must equal the thickness penetrated:

$$\mathcal{R}_{Z,M}\,(E/M) - \mathcal{R}_{Z,M}\left(E'/M\right) = L\ , \tag{1}$$

where the function $\mathcal{R}_{Z,M}$ is available in tabulated form (see, for example, Hubert et al., 1990). Thus from measurements of E', $\Delta E = E - E'$, and L this fundamental

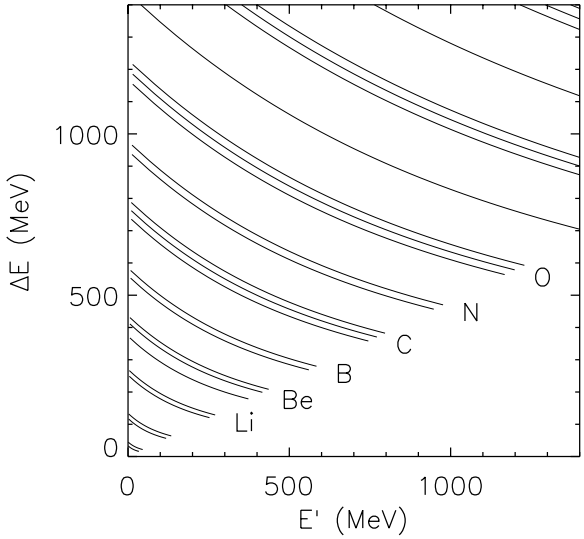

Figure 5. Calculated relationship between energy loss (ΔE) and residual energy (E') for nuclei penetrating a 6 mm silicon detector and stopping in the following 6 mm detector. Each curve corresponds to a different stable or long-lived nuclide. Selected elements are labeled. The locations of the response tracks also depend on the angle of incidence. An approximate correction for this dependence can be made by dividing both ΔE and E' by $(\sec\theta)^{1/a}$ where $a \simeq 1.7$.

equation of the 'ΔE–E' technique' provides information about a particle's charge and mass. An iterative technique for solving this equation is discussed by Stone et al. (1998). Figure 5 illustrates the ΔE vs E' relationship expected for isotopes of several elements when the energy loss is measured in a 6 mm thick layer of silicon.

Further insight into this method can be obtained by introducing an approximate power-law form for the range–energy function, $\mathcal{R}_{Z,M}(E/M) \simeq k(M/Z^2)(E/M)^a$. This form, with $a \simeq 1.7$, is a reasonable approximation to the range–energy relation over much of the energy interval of interest for CRIS. Substituting the power-law form of the range–energy relation into Equation (1) and solving for mass one obtains:

$$M \simeq \left(k/Z^2L\right)^{1/(a-1)} \left(E^a - E'^a\right)^{1/(a-1)} . \tag{2}$$

Similarly, by assuming a nominal mass-to-charge ratio typical of the elements of interest, $M/Z \simeq 2 + \epsilon$, one can also solve for the charge:

$$Z \simeq \left(\frac{k}{L\,(2+\epsilon)^{(a-1)}}\right)^{1/(a+1)} \left(E^a - E'^a\right)^{1/(a+1)} . \tag{3}$$

From these equations one can readily show that the spacing between 'tracks' for adjacent elements on the ΔE–E' plot is larger than the spacing between adjacent isotopes of an element by a factor $(2+\epsilon)(a+1)/(a-1) \simeq 8$. For elements with

$Z \leq 30$ the number of stable or long-lived isotopes is small enough that one never encounters an ambiguity in the identification of charge and mass. In practice, one first calculates the particle's charge. A histogram of the resulting values for a population of particles yields well-separated element peaks. Identification of these peaks gives the integer charge values needed for the mass calculation.

The approximate expressions for charge and mass (Equations (2) and (3)) are also helpful for assessing the importance of various sources of uncertainty in ΔE, E', and L. For example, since $M \propto L^{1/(a-1)}$, one sees that a fractional error σ_L/L in the penetrated thickness contributes a fractional uncertainty in the mass $(\sigma_M/M)_L = (\sigma_L/L)/(a-1)$. For iron, this implies that to keep the contribution to the mass uncertainty from thickness errors to less than 0.1 amu, one needs to determine the thickness to ~0.12% or better. Since CRIS is designed to measure particles incident over a wide range of angles, the value of L depends not only on the detector thickness (denoted by L_0), but also the angle of incidence, θ: $L = L_0 \sec\theta$. To provide the necessary determination of θ, CRIS includes a sensor system capable of precisely measuring particle trajectories. Furthermore, the detector thicknesses are not perfectly uniform and it is necessary to apply maps of the measured thickness as a function of location on the detector. The trajectory system also provides the event-by-event location information needed to make these mapping corrections.

In CRIS there is the additional complication that the detectors have significant surface 'dead layers' in which energy lost by a particle will not contribute to the measured pulse height (see Section 4.2). Equation (1) can be generalized to take these dead layers into account (see Appendix A). Maps of measured dead layer thickness are used to correct for the spatial dependence of this quantity.

Even when the quantities ΔE, E', L_0, and θ are well determined there are important contributions to the mass resolution caused by several physical sources of fluctuations occurring as particles slow in matter. Most important among these are Bohr/Landau fluctuations of the energy loss in the ΔE detector (Rossi, 1952) and multiple Coulomb scattering (Barnett, 1996), which causes the particle's path to deviate from the straight line derived from the trajectory measurements. One strives for an instrument design in which the mass resolution is dominated by these fundamental contributions.

Appendix A discusses the various contributions to the mass resolution, and Section 8.3 presents the overall mass resolution calculated for selected elements using the parameters of the CRIS instrument.

3.2. DETAILED REQUIREMENTS

The development of a CRIS 'error budget' that would make it possible to achieve the required overall mass resolution $\lesssim 0.25$ amu led to specific design requirements on a number of the subsystems of CRIS. These included requirements on (1) the gain, linearity, noise, stability, and dynamic range of the pulse-height analysis

electronics; (2) the leakage current, thickness uniformity, and dead layers of the solid-state detectors; (3) the position and angular resolution of the trajectory system; and (4) the alignment and stability of the mechanical design. In addition to these design requirements, it became clear that to achieve optimal mass resolution required mapping the thickness and dead layers of each of the individual solid-state detectors to an accuracy of a few μm, and it required accelerator calibrations of the completed instrument.

Table III summarizes the requirements that were adopted and that guided the design and development of the CRIS instrument. The following sections describe the instrument that was designed to meet these requirements, and present the results of calibrations and calculations used to demonstrate that the intended performance has been achieved.

4. Sensor System

The CRIS sensor system consists of a scintillating optical fiber trajectory (SOFT) hodoscope for measuring the location and direction of incidence of detected nuclei, and four silicon solid-state detector telescopes for measuring the energy loss signatures of these particles. Figure 6 schematically shows the configuration of the instrument. Figure 7 contains a photograph of the fully assembled CRIS instrument. The SOFT hodoscope is described in Section 4.1 and the silicon detector telescopes are discussed in Section 4.2.

4.1. The scintillating optical fiber trajectory (SOFT) system

The SOFT system (Figure 6) consists of a hodoscope composed of three xy scintillating fiber planes (six fiber layers) and a trigger detector composed of a single fiber plane (two fiber layers). The hodoscope and trigger fibers are coupled to an image intensifier which is then coupled to a charge-coupled device (CCD) for hodoscope readout, and to photodiodes to obtain trigger pulses. The SOFT detector system has two fully redundant image-intensified CCD camera systems viewing opposite ends of the fibers. Only one of these camera systems is operated at any given time because of power and bit rate limitations. Figure 8 is a photograph showing the internal layout of the SOFT system.

4.1.1. *Scintillating Fiber Hodoscope*

The scintillating fibers consist of a polystyrene core doped with scintillation dyes (BPBD and DPOPOP, emission peak 430 nm (Davis et al., 1989)) surrounded by an acrylic cladding. These fibers, fabricated by Washington University, have a 200 μm square cross section which includes a 10 μm cladding thickness on each side. The cladding of the hodoscope fibers is coated with a black ink (called 'extramural absorber' or EMA) to prevent optical coupling between fibers. The fibers are

TABLE III
CRIS design requirements

Parameter	Requirement
Trajectory system	
Zenith angle resolution	$<0.1°$
Relative position resolution	<0.13 mm r.m.s.
Absolute position resolution	<1 mm r.m.s.
Detection efficiency	
$Z = 4$ (Be)	$>50\%$
$Z \geq 8$	$>90\%$
Silicon detectors	
Active thickness	3.0 ± 0.1 mm
Thickness variation	<60 μm
Dead layer thickness	$\lesssim 50$ μm
Depletion voltage	<250 V
Leakage current (20 °C)	<15 μA
Pulse-height analyzer electronics	
Dynamic range	>700:1
Quantization resolution	12 bits or better
Nonlinearity	$<0.05\%$
Gain temperature coefficient	<200 ppm/°C
Offset temperature coefficient	<200 ppm/°C
Ballistic deficit	$\lesssim 0.2\%$
Noise (r.m.s., for guards)	<50 keV
Power (per pha)	<100 mW
Mechanical construction	
Lateral position tolerance	
Trajectory system	0.25 mm plane-to-plane
	1 mm with respect to Si detectors
Silicon detectors	1 mm detector-to-detector
Orientation co-planarity	
Trajectory system	0.1°
Silicon detectors	0.1°
Detector azimuthal orientation	
Trajectory system	0.1° plane-to-plane
	1° with respect to Si detectors
Silicon detectors	1° detector-to-detector

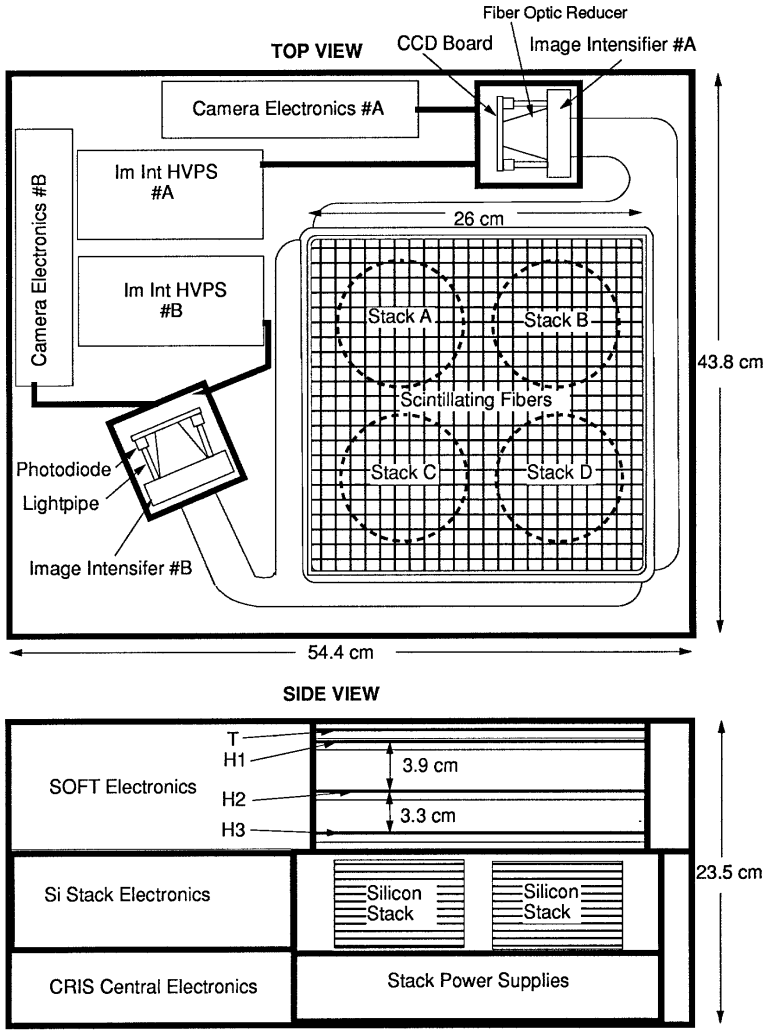

Figure 6. CRIS instrument cross section. The side view shows the fiber hodoscope which consists of three hodoscope planes (H1, H2, H3) and one trigger plane (T) which are located above the four stacks of silicon detectors. The top view shows the fiber readout which consists of two image intensified CCDs at either end of the fibers and the four stacks of silicon detectors.

bonded together with an elastomeric adhesive (Uralane 5753). Each of the three hodoscope planes is composed of two layers of orthogonally crossed fibers. The fiber planes are constructed by mounting one layer (or ribbon) of fibers, which is 26 cm wide and about 125 cm long, onto a 25 μm thick Kapton substrate which has been stretched on a square cross-section frame with outside dimensions of 28 cm$\times$28 cm. A second fiber layer is then mounted orthogonal to the first layer to form an xy plane. Uralane adhesive is used to bond the first layer to the Kapton substrate and the second layer to the first layer. The second layer also has a thin

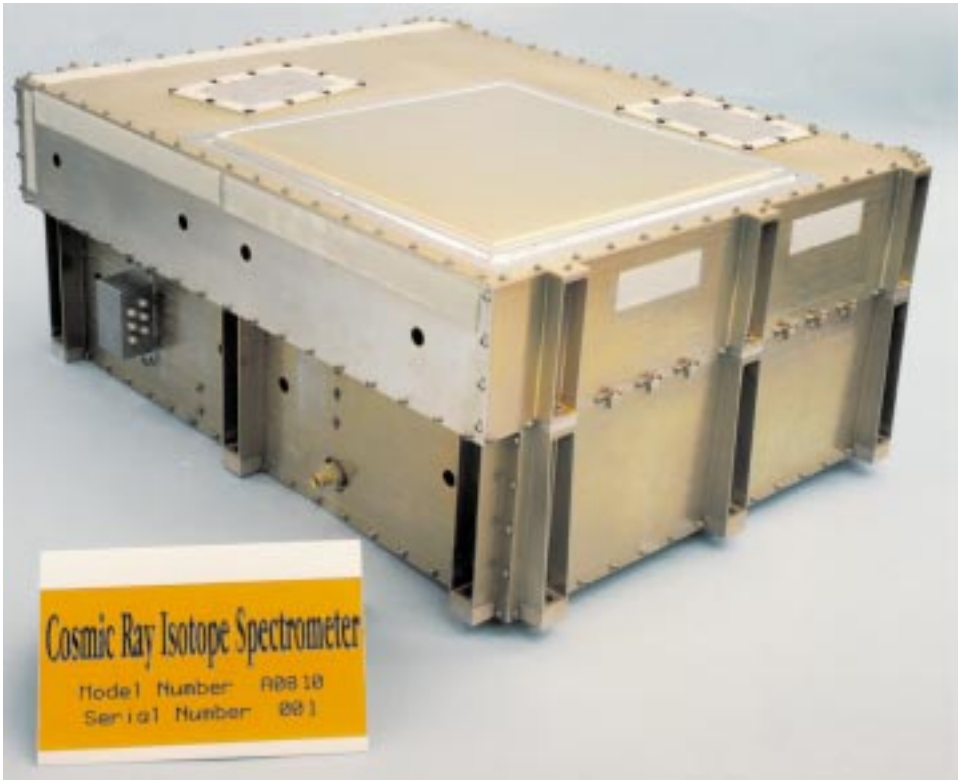

Figure 7. Fully assembled CRIS instrument consists of two boxes bolted together. The upper box contains the SOFT system, while the lower box contains the Si(Li) detector stacks with their pulse-height analysis electronics, as well as the main CRIS control electronics. The large window on the top of the SOFT box is the CRIS entrance aperture. The two smaller patches are thermal radiators for cooling the two CCD cameras.

coating of adhesive on top which completes the encapsulation of the fibers. The crossed-fiber planes form an active region 26 cm$\times$26 cm centered on the frame and Kapton substrate, with approximately a 50 cm length of fibers on either end of each layer to light pipe the photons to the two image intensifier assemblies (Figures 6 and 8).

The spacings between the hodoscope planes are 3.9 cm and 3.3 cm for H1–H2 and H2–H3, respectively. (This unequal plane spacing is used to resolve trajectory ambiguities which can occur for low-Z nuclei due to electron 'hopping' in the intensifier, as discussed in Section 9.3.) Each of the four 26 cm wide hodoscope fiber outputs for a plane is split into 11 'tabs' with width $\sim$2.4 cm of contiguous fibers (about 120 fibers). The tabs are then stacked together with a spacer of thickness 50 μm placed between each tab at the end of the ribbon. The tabs with spacers are bonded together forming four rectangular outputs for each plane with dimensions $\sim$0.3 cm$\times$ $\sim$2.4 cm.

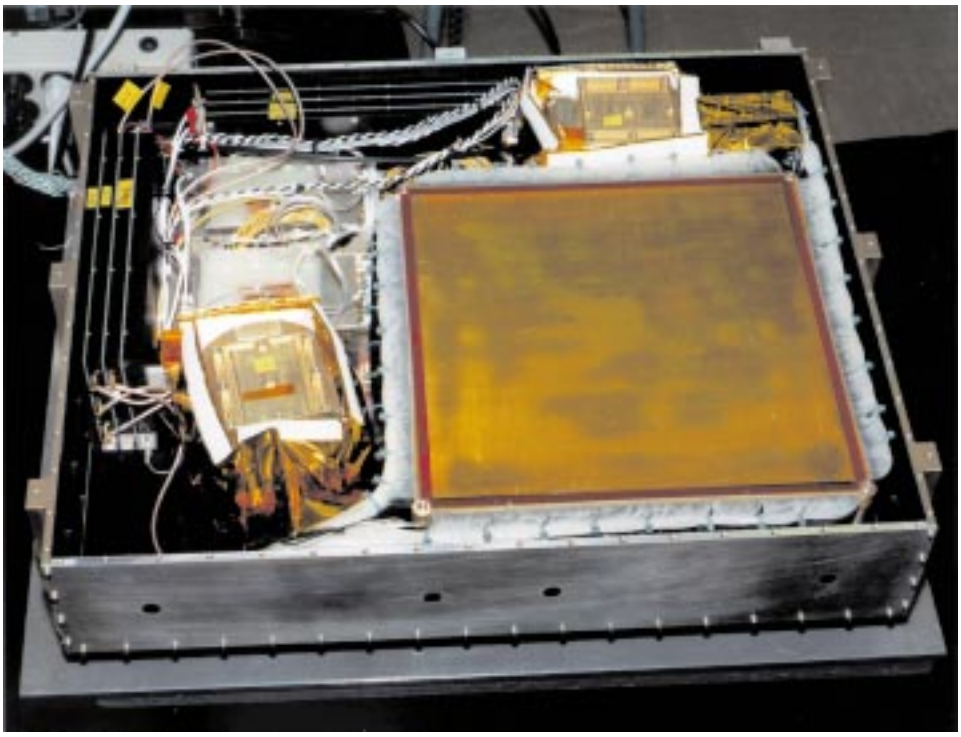

Figure 8. Photograph showing a top view of the SOFT detector before integration with the rest of the CRIS instrument. The fiber plane which is visible is the trigger plane. The hodoscope planes are below that and are not visible. The fiber outputs are routed to two image intensifier/CCD assemblies, one at the upper right and one at the lower left of the photo. Thermal radiators are attached to the tops of the assemblies in flight (not shown in this photo, see Figure 7) to cool the image intensifiers and CCD arrays. The high-voltage power supplies for the image intensifiers are located to the upper left of the fiber plane. The readout electronics for each camera are in the black boxes in the upper left of the photograph.

Each of the two sets of six fiber layer outputs (denoted H1x, H1y, H2x, H2y, H3x, and H3y) is routed to one of the image intensified CCD cameras. The six outputs are stacked as illustrated in Figure 9, and clamped together forming a block which is then cut and polished and coupled to the image intensifier using Dow-Corning 93-500 adhesive with thickness $\sim$50 μm. This thickness was necessary to eliminate flashes in the image intensifier caused by electrostatic buildup between the plastic fibers and the image intensifier faceplate. The bundle of fibers running from the active area to the image intensifier was then encapsulated with Uralane.

The trigger fiber plane is fabricated in the same way as the hodoscope planes with the exception that the fibers are not coated with EMA so that maximum sensitivity can be obtained. The trigger fiber outputs are formatted similarly to the hodoscope fibers with the x-layer outputs being placed above and the y-layer outputs placed below the hodoscope outputs on the face of the image intensifier.

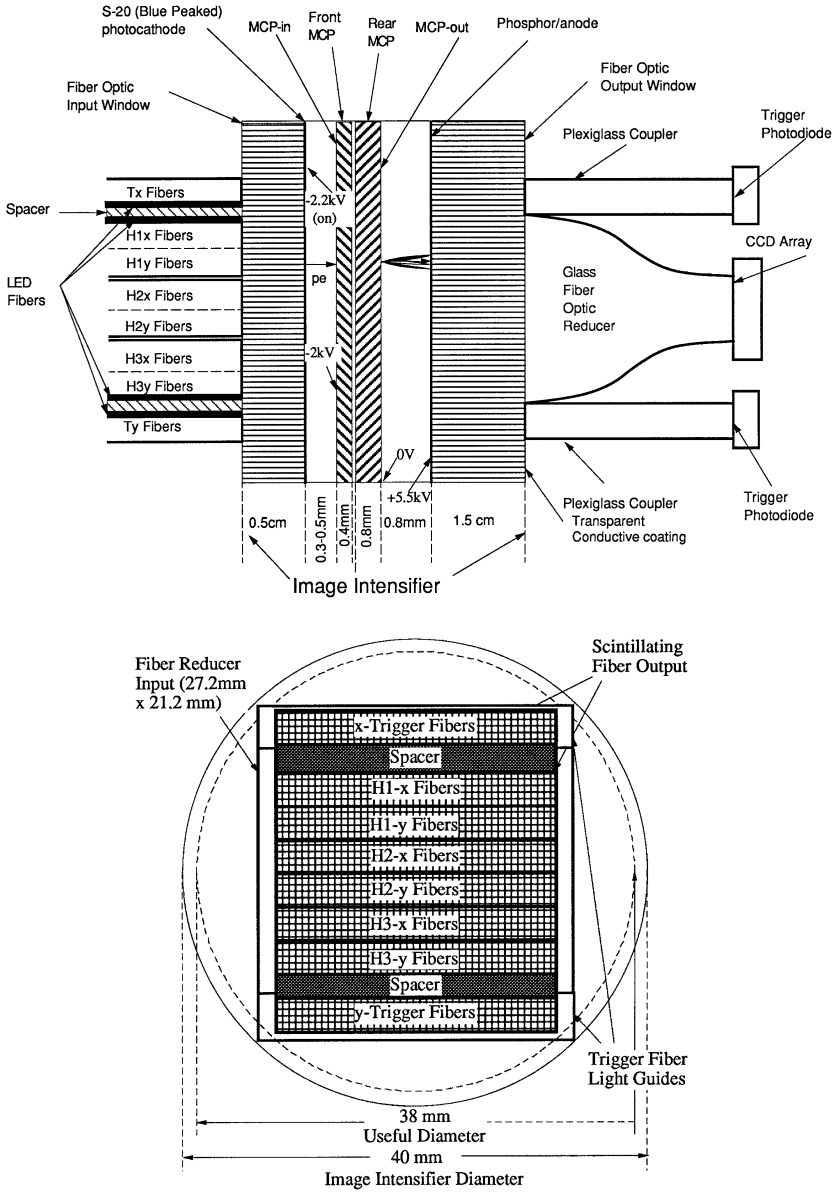

Figure 9. Schematic view of SOFT image intensified CCD camera. The top section of the figure shows a side view of the fiber readout. The scintillating fibers are shown on the left of the image intensifier and are proximity focused onto the fiber-optic face plate of the image intensifier. At the output of the image intensifier the hodoscope fibers (H1–H3) are fiber-optic reduced onto the CCD for readout. The trigger fibers (Tx and Ty) are interfaced with a Plexiglass coupler to photodiodes which produce signals used in the CRIS coincidence determination. The bottom section of the figure shows a face view of the fibers as they are formatted onto the image intensifier. The hodoscope fibers are formatted into the center of the image intensifier and the trigger fibers are spaced off at the top and bottom from the hodoscope fibers so that their output is clearly separated. The fiber reducer input (output of the image intensifier), which proximity focuses the image onto the CCD, and the trigger fiber light guides are also shown.

TABLE IV
Materials in cosmic-ray beam path[a]

Item	Material	Composition	Thickness[b] (mm)	Areal density[b] (g cm^{-2})
MLI thermal blanket	Multiple material types			0.083
Entry window	Aluminum	Al	0.254	0.069
Trigger fiber plane	Polystyrene	C_8H_8	0.324	0.033
	Acrylic	$C_5H_8O_2$	0.076	0.009
	Uralane 5753		0.175	0.018
	Kapton	$C_{22}H_{10}O_5N_2$	0.025	0.004
H1 fiber plane	— same as trigger fiber plane —			0.064
H2 fiber plane	— same as trigger fiber plane —			0.064
H3 fiber plane	— same as trigger fiber plane—			0.064
Exit window	Aluminum	Al	0.127	0.034
			Total:	0.442

[a]Above the silicon detector stacks.
[b]Average over active area.

Spacers are placed between the hodoscope and trigger fiber outputs as shown in Figure 9 to clearly separate the readout of hodoscope and trigger fibers.

Four extra tabs of fibers which are not part of the hodoscope or trigger planes are placed above and below the trigger fiber spacers (for each camera) and are attached to LEDs. These are used for functional testing and alignment checks of the system. Five groups of several fibers in each of the four tabs are attached to the LEDs.

Table IV lists the areal density of materials in SOFT including the thermal insulation and entry window dome as well as the thin aluminum sheet separating the fiber detector from the silicon stack detectors. The SOFT hodoscope is a self-contained assembly which can be tested independent of the rest of the CRIS instrument.

4.1.2. *Image Intensifier Assembly*

A cross-sectional view of the image intensifier assembly is shown in Figure 9. The image intensifiers are 40 mm diameter, dual microchannel plate (MCP), gateable devices (Photek Model MCP-340S). The rear MCP is double thickness (0.8 mm) so that the gain provided by the tube is equivalent to that for a three-MCP intensifier. The tubes are each powered by a high-voltage power supply (Model 2404) made by K&M Electronics. The intensifiers have fiber optic faceplates on the input and output. The blue peaked, S-20 photocathodes have a sensitivity of $\sim$50 mA W^{-1} at 450 nm wavelength (roughly 15% quantum efficiency).

The intensifiers exhibit about 20 to 30 dark counts cm^{-2} s^{-1} at room temperature and a much smaller rate at temperatures of $\lesssim$0 °C. The vacuum side of the

fiber optic output window is coated with P-20 phosphor and a thin film aluminum anode is deposited over the phosphor. The phosphor has an e^{-1} decay time of about 50 μs, with a low level tail extending for about 1 ms. The external face of the output window is coated with a thin, optically transparent metallic layer which is grounded to prevent corona from the anode. The internal structure of the image intensifier was ruggedized to ensure that it would survive the vibration and shock levels expected in the ACE launch environment.

The voltages used to power the intensifier are indicated in Figure 9. The MCP-out is held at signal ground, the anode is at +5.5 kV, and the MCP-in is variable from zero to −2 kV. The cathode is held at a voltage with respect to the MCP-in of −200 V when it is gated on and a voltage of +40 V when it is gated off. The gating, which can be accomplished in ∼1 μs, is used to turn off the image intensifier during event readout. The variable MCP-in voltage allows the overall image intensifier gain to be controlled during flight up to a maximum photon gain of $\sim 2 \times 10^6$. The region of the image intensifier output corresponding to the hodoscope fiber input is coupled onto the large end of a 34.5 mm to 11 mm (diagonal dimension, 3:4 aspect ratio) fiber-optic reducer* with Dow-Corning 93-500 adhesive. The reducer output is coupled with Uralane adhesive to a fiber optic window installed on the CCD. The Thompson TH-7866 CCD is a 244 × 550 array with individual pixel size 16 μm (width) × 27 μm (height). A single fiber projects onto an area 4 pixels wide by 2.4 pixels high, after image reduction by the fiber optic reducer. The regions of the image intensifier output corresponding to the two trigger fiber inputs are coupled to Hamamatsu S-3590-01 photodiodes using acrylic light guides. The CCD and photodiodes are mounted on a circular printed circuit board located at the back of the image intensifier assembly.

The image intensifier assembly is thermally isolated from the rest of the SOFT detector by multi-layer insulation (MLI) blankets and thermal standoffs at all mounting points. The top of each assembly is attached to a radiator (Figure 7; two small rectangular plates on top of CRIS) which views space and is designed to provide cooling to ~ -20 °C in flight. From accelerator tests it has been shown that by operating at ∼0 °C and shuttering the camera as described in Section 5.3 (∼100 ms shutter speed) there is negligible background from thermal photoelectron emission ($\ll$1 photoelectron frame^{-1}) and CCD dark current build-up. Heaters are provided to maintain the temperature above −25 °C, thus minimizing thermally induced stresses in the assembly. The outer housing of the image intensifier is 1 cm thick aluminum to reduce radiation damage to the CCD.

4.2. SILICON DETECTOR TELESCOPES

Energy losses of particles detected in CRIS are measured in detector 'telescopes' consisting of stacks of 15 silicon detectors. As indicated in Figure 6, CRIS contains four detector telescopes to achieve a large collecting area and to provide redun-

* The SOFT fiber-optic reducer was produced by Schott Fiber Optics.

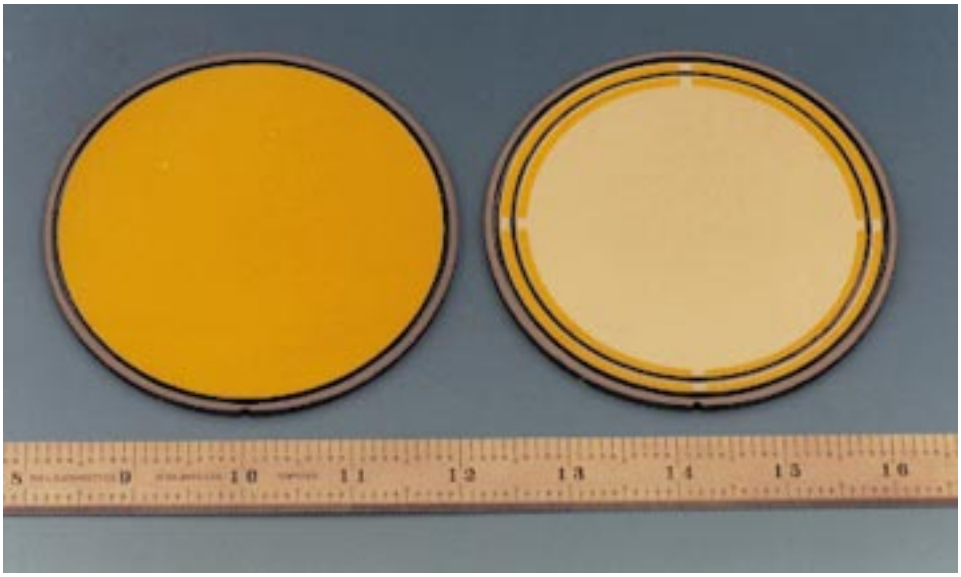

Figure 10. Photographs of CRIS stack detectors. A single groove detector is on the left, and a double groove is on the right. The silicon wafers are 10 cm in diameter and 3 mm thick. The annular region between grooves of the double-groove detector serves as an active guard region for identifying particles which exit or enter through the sides of the stack.

dancy. The individual detectors are made from silicon wafers 10 cm in diameter and 3 mm thick. These thick wafers are processed using lithium compensation technology (Allbritton et al., 1996) to produce a large volume of material with effective impurity concentrations approaching those of intrinsic silicon. The lithium-drifted silicon detectors, denoted Si(Li), that are produced from this compensated material can be thick (several millimeters) yet be fully depleted using relatively modest bias voltages. All CRIS detectors use −400 V bias, applied to the ungrooved surface.

The Si(Li) detectors in CRIS are made in two different designs, as shown in Figure 10. In one design a single groove, concentric with the wafer, has been cut into one of the surfaces. This groove separates the central active region of 68 cm^2 area from an inactive outer ring which is used for physically mounting the detector. The other design has two concentric grooves. The outer groove is identical to those in the single-groove devices, while the inner groove separates the active region of the detector into a central region of 57 cm^2 area surrounded by an annular 'guard ring'.

Each telescope contains four single-groove detectors and 11 double-groove devices arranged as shown in Figure 11. The designations used for each of the detectors are indicated in this figure. Events best suited for mass analysis involve nuclei which enter the telescope through the top of E1, penetrate the central regions of a number of subsequent detectors, and come to rest somewhere between E2 and E8, inclusive. For nuclei which exit from the telescope before stopping, the total energy

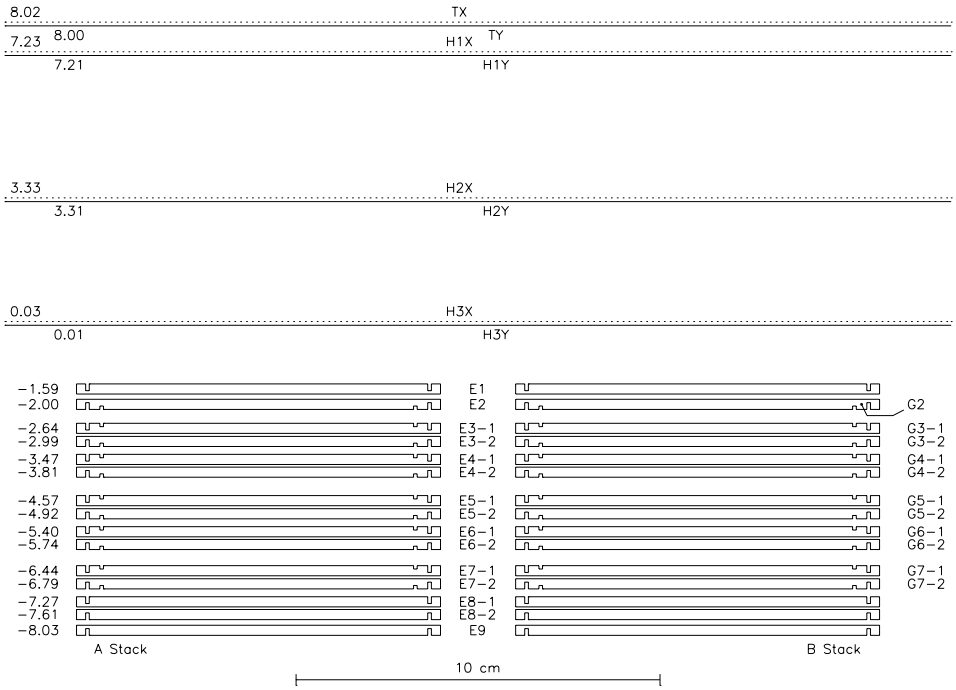

Figure 11. Cross section of the CRIS sensor system in a plane passing through the centers of the A and B detector stacks. The designations used for each sensor element are indicated: TX and TY are the SOFT trigger planes, H1X through H3Y are the SOFT hodoscope planes, E1 through E9 are the central regions of the Si(Li) detectors, and G2 through G7-2 are the guard rings of the double-groove detectors. The dimensions indicated on the left side of the figure show the locations of the top surface of each sensor, measured in cm from an origin chosen near the bottom of the SOFT system.

is not directly measured and the particle identification is less accurate. Particles which exit through the back of the telescope are indicated by an energy loss in E9, while those which exit through the sides are flagged by a signal in one or more of the guard regions. The guards G2 through G7 together with the E9 detector serve as an active anticoincidence which can flag a large fraction of exiting particles, allowing them to be discarded and thus preserving the limited telemetry for higher priority events. Two different guard threshold settings are implemented. For nuclei heavier than helium a high-level guard signal is used to veto an event on board, but a low-level guard signal is simply included in the event telemetry for processing on the ground. This approach assures that a small component of cross-talk between center and guard regions of a detector will not cause the loss of good events.

A fraction of the nuclei which exit through the sides of a stack pass through the gaps between the individual guards and are not identified on board. These events, which mainly occur at wide angles, are processed as though they were due to stopping particles, but are subsequently identified on the ground and discarded based on their trajectory and their pattern of energy losses in the penetrated detectors.

4.2.1. *Si(Li) Detector Fabrication*

Fabrication of Si(Li) detectors began with p-type silicon crystals having resistivity in the range ∼1–3 kΩ cm. Topsil Semiconductor Materials produced silicon ingots having the necessary characteristics by controlled gas-phase doping of the material with boron during the float-zone refining process used to purify the silicon and grow the crystal (⟨111⟩ orientation). The resulting silicon rod was subsequently machined down to 10 cm diameter and cut into slices. After lapping to the specified thickness, the silicon wafers were delivered to the Lawrence Berkeley National Laboratory (LBNL) for detector fabrication.

At LBNL the silicon wafers were processed into large area diodes. Lithium was vacuum deposited on one surface and diffused into the top several hundred microns of the silicon, forming a thick n^+ contact on the p-type wafer. Grooves of width ∼1 mm and depth ∼1.5 mm were then ultrasonically cut into the lithiated surface to define the boundaries of the central active region and the guard ring. (A passivating layer of photoresist was later applied in these grooves.)

Acceptor impurities in the crystal were compensated by drifting lithium through the wafer, a process which was performed under carefully controlled temperature, voltage, and current conditions. The lithiated surface was then lapped down to reduce the thickness of the dead layer. The sheet resistance of this surface was monitored and the thinning was stopped when this value had increased to ∼20 Ω per square. Metallic contacts were vacuum deposited on the detector faces: aluminum on the junction (grooved) surface and gold on the ohmic (ungrooved) surface. Subsequently, additional metallization (chromium plus gold) was added in selected areas over the aluminum to reduce the resistance and improve the reliability of the electrical contacts to the detector (see Section 6).

A small notch was cut into the edge of each detector in a fixed orientation relative to the crystal axes in order to facilitate aligning and locking the detectors in their modules, as discussed in Section 6. This careful alignment was motivated by observations made during accelerator calibrations of degraded resolution for particles with certain angles of incidence relative to the crystal axes.

Further details of the Si(Li) detector design and fabrication can be found in Allbritton et al. (1996) and Dougherty et al. (1996).

4.2.2. *Detector Performance Testing*

After fabrication, electrical characteristics of the detectors were measured at LBNL to identify devices which did not meet specifications. (Many of these were subsequently reprocessed and yielded good detectors.) Measurements included: (1) depletion bias, as determined by obtaining full pulse height for alpha particles incident from the ohmic surface of the detector; (2) leakage current measured at room temperature; and (3) room temperature noise measured using pulse shaping comparable to that in the flight instrument. The leakage current and noise are generally correlated, since for the CRIS detectors the room temperature noise tends to be dominated by the fluctuations in the leakage current (shot noise). However,

bad detectors were often identifiable from noise levels significantly exceeding the expected shot noise. In addition to the above tests, which were performed in air, detectors were briefly checked in vacuum to identify any devices which would become unstable under vacuum conditions. Detectors which passed this suite of tests were delivered to the CRIS instrument team for more extensive testing.

At GSFC and Caltech, the detectors were tested in vacuum at temperatures near −25 °C, 20 °C, and 35 °C. These tests, which typically lasted 3 to 4 weeks, were intended to check the stability of the detector noise and leakage current under the range of conditions expected in flight. Most of this time was spent at the warmest temperature since previous experience indicated that most stability problems are encountered under warm conditions. In these thermal-vacuum (TV) tests, an automated data-acquisition system collected noise and leakage-current data for each detector every few minutes. These measurements made it possible to identify detectors subject to intermittent periods of elevated noise, even of relatively short duration. In addition, the TV tests showed that most of the CRIS detectors experienced gradual leakage current growth in vacuum (but not in air) with typical initial rates of ∼2% per day. Concerns over the implications of this growth for the CRIS instrument lifetime prompted more extensive TV testing of a few detectors. These tests, carried out at a temperature ∼8 °C, more characteristic of temperatures expected in flight, extended over more than 6 months. It was found that the leakage current growth is less (in % per day) at the lower temperature, and that the current gradually stabilizes over several months of operation.

Table V summarizes the measured characteristics of the CRIS Si(Li) detectors.

4.2.3. *Thickness and Dead Layer Mapping*

At LBNL, the thicknesses of the Si(Li) detectors were measured at 24 points distributed over the central active region using a non-contact technique in which capacitance measurements were used to determine the residual air gap that remains when a conductor (the detector with its surface contacts grounded) is placed between a pair of probes. The capacitance gauge measurements were converted to absolute thicknesses by comparing with similar measurements made on a gauge block of precisely known thickness. Average detector thicknesses were found to lie in the range 2918 to 3027 μm, with a mean of 2990 μm.

In order to obtain detailed thickness maps covering the entire central active area, measurements were made using a beam of 100 MeV nucl^{-1} ^{36}Ar nuclei from the National Superconducting Cyclotron Laboratory (NSCL) at Michigan State University (MSU). In these runs the beam penetrated the detector of interest and stopped in a second detector placed behind it. This detector pair was scanned using a small (∼1 cm diameter) beam spot and the pulse heights were recorded as a function of position on the detector using particle trajectory information accurate to ∼1 mm obtained from a set of multiwire proportional counters. The residual energy signal from the back detector (E') provided a measure of the variation of the total thickness of the front detector (ΔE). By correlating E' values with absolute

TABLE V
Si(Li) detector characteristics

Parameter	Typical values[a]	Notes
Depletion voltage (V)	110 ± 40	a few values up to 230 V
Operating voltage (V)	400	
Noise (keV FWHM)	150 ± 50	20 °C, 2.4 μs peaking time
Leakage current (μA)		20 °C
Single-groove detectors	11 ± 4	
Double-groove detectors	17 ± 3	center and guard connected
Initial leakage current growth (% day^{-1})	2.0 ± 1.5	20 °C in vacuum
Average thickness (μm)	2970 ± 55	2990 μm average
Maximum thickness gradient (μm mm^{-1})	1.0 ± 0.25	
Average dead layer thickness (μm)	60 ± 30	lithiated surface
Central active area (cm^2)		
Single-groove detectors	68	
Double-groove detectors	57	

[a] '$\pm$' indicates typical range of values, not uncertainty.

thicknesses from capacitance gauge measurements at the same locations, full-area maps of absolute thickness were obtained.

The sum of the ΔE and E' signals measures the dead layer. The deduced dead layers are consistent with the expected thickness of heavily lithiated silicon, $\sim$55–70 μm, calculated from the detector fabrication parameters. In using the accelerator data to derive the dead layer thickness, it was assumed that no signal is collected from the ionization produced in the dead layer, while collection of ionization charge from the rest of the detector is 100% efficient. However, our measurements with alpha particles incident through the dead layer show that there is partial efficiency for collection of the ionization signal from this layer, presumably as a result of some charge diffusing out of the layer before it can be lost to recombination. This feature is likely to be significant only for nuclei that stop in or very near the dead layer.

Figure 12 shows an example of a thickness map and a dead-layer map derived from the accelerator measurements, and Table V lists the range of thicknesses and gradients that were obtained for the flight detectors.

4.2.4. *Pulse-Height Analysis of Stack Detectors*

The energy losses of particles entering the CRIS stacks are precisely measured using custom integrated-circuit pulse-height analyzers (PHAs) described in Section 5.2. Because of the large number of signals available from the CRIS Si(Li) detectors (60 centers and 44 guards), selected sets of detectors are connected in

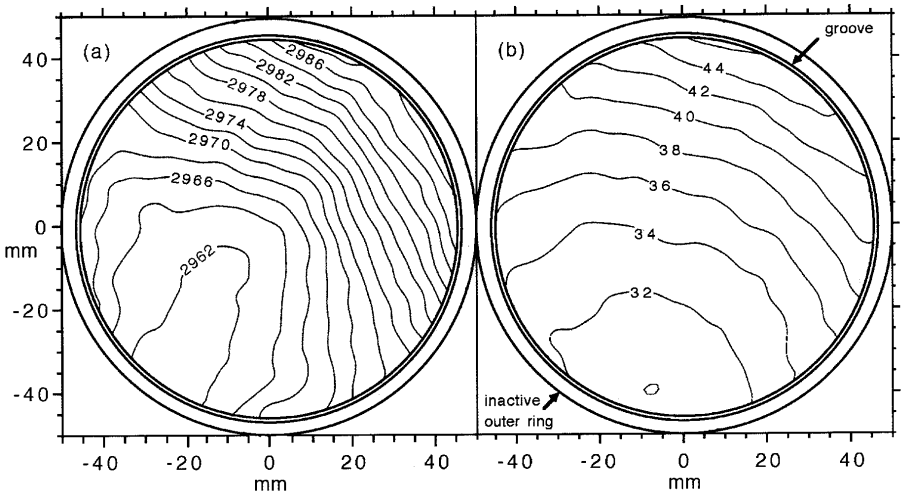

Figure 12. Contour plots of thickness (a) and dead layer (b) for a CRIS stack detector. Dead layers and relative thicknesses were derived from measurements made using beams of ^{36}Ar ions at an energy of 100 MeV nucl^{-1} from the MSU/NSCL cyclotron. Absolute thicknesses were obtained with a capacitance thickness gauge (see text). Contours are labeled in units of μm. In this example the dead layer is somewhat less than the typical value of $\sim$60 μm.

parallel for pulse-height analysis to reduce the complexity of the electronics. The detectors within a stack are labeled as indicated in Figure 11, while the four stacks are designated by the letters A, B, C, and D. Thus, for example, the first detector in stack A is called E1A. All four of the E1 detectors are individually pulse-height analyzed. However, the signals from E2A and E2B are summed into one single PHA, and the signals from E2C and E2D are summed into another. Table VI shows the combinations of detector signals that are summed in each of the 32 PHAs in CRIS. The letter 'G' denotes the guard ring of the detector.

5. Electronics and Onboard Data Processing

The CRIS instrument is functionally and electronically divided into the SOFT and 'stack' sections, allowing for parallel development and test programs. The main electronics card cage is contained in the stack section and houses all subsystems (low- and high-voltage power, logic and microprocessor, stack-detector readout circuits, analog DC control voltage generation circuitry, and housekeeping monitors) except those directly associated with the SOFT system (CCD cameras, image intensifier tubes and associated high voltage, and camera readout and data compression circuitry). The electronics design combines established and new circuit and packaging technologies with the goal of enhancing serviceability, reliability, and performance, within the confines of an aggressive development schedule. Notable design features include:

TABLE VI
Pulse-height analyzers and bias supplies

PHA label	Bias[a]	Detector elements	PHA label	Bias[a]	Detector elements
E1A	1	E1A	E1C	3	E1C
E1B	2	E1B	E1D	4	E1D
E2AB	1	E2A E2B	E2CD	3	E2C E2D
E3AB	1	E3-1A E3-2A E3-1B E3-2B	E3CD	3	E3-1C E3-2C E3-1D E3-2D
E4AB	1	E4-1A E4-2A E4-1B E4-2B	E4CD	3	E4-1C E4-2C E4-1D E4-2D
E5AB	1	E5-1A E5-2A E5-1B E5-2B	E5CD	3	E5-1C E5-2C E5-1D E5-2D
E6AB	2	E6-1A E6-2A E6-1B E6-2B	E6CD	4	E6-1C E6-2C E6-1D E6-2D
E7AB	2	E7-1A E7-2A E7-1B E7-2B	E7CD	4	E7-1C E7-2C E7-1D E7-2D
E8AB	2	E8-1A E8-2A E8-1B E8-2B	E8CD	4	E8-1C E8-2C E8-1D E8-2D
E9AB	2	E9A E9B	E9CD	4	E9C E9D
G2AB[b]		G2A G2B	G2CD[b]		G2C G2D
G3AB[b]		G3-1A G3-2A G3-1B G3-2B	G3CD[b]		G3-1C G3-2C G3-1D G3-2D
G4AB[b]		G4-1A G4-2A G4-1B G4-2B	G4CD[b]		G4-1C G4-2C G4-1D G4-2D
G5AB[b]		G5-1A G5-2A G5-1B G5-2B	G5CD[b]		G5-1C G5-2C G5-1D G5-2D
G6AB[b]		G6-1A G6-2A G6-1B G6-2B	G6CD[b]		G6-1C G6-2C G6-1D G6-2D
G7AB[b]		G7-1A G7-2A G7-1B G7-2B	G7CD[b]		G7-1C G7-2C G7-1D G7-2D

[a]Four bias supplies are shared among the 60 detectors, as indicated. Separate switches allow bias to be disconnected from the set of detectors connected to any center PHA.
[b]Detectors are biased on the ungrooved surface. Guard regions have the same bias as the corresponding central regions.

(1) The use of Actel A1020 field programmable gate arrays for essentially all logic functions.

(2) A card cage/backplane packaging concept using thermally actuated zero-insertion-force connectors.

(3) Modular packaging of the stack detectors onto the same removable printed circuit boards that carry the front-end readout electronics.

(4) A complete pulse-height analyzer hybrid circuit in which all active components reside on a custom bipolar VLSI chip.

(5) A radiation-hard microprocessor system based on the RTX2010, programmed in Forth, for low power, yet high performance real-time hardware control and data processing.

Sections 5.1–5.3 discuss individual subsystems of the CRIS electronics, while Sections 5.4 and 5.5 describe the on-board data processing and commanding functions.

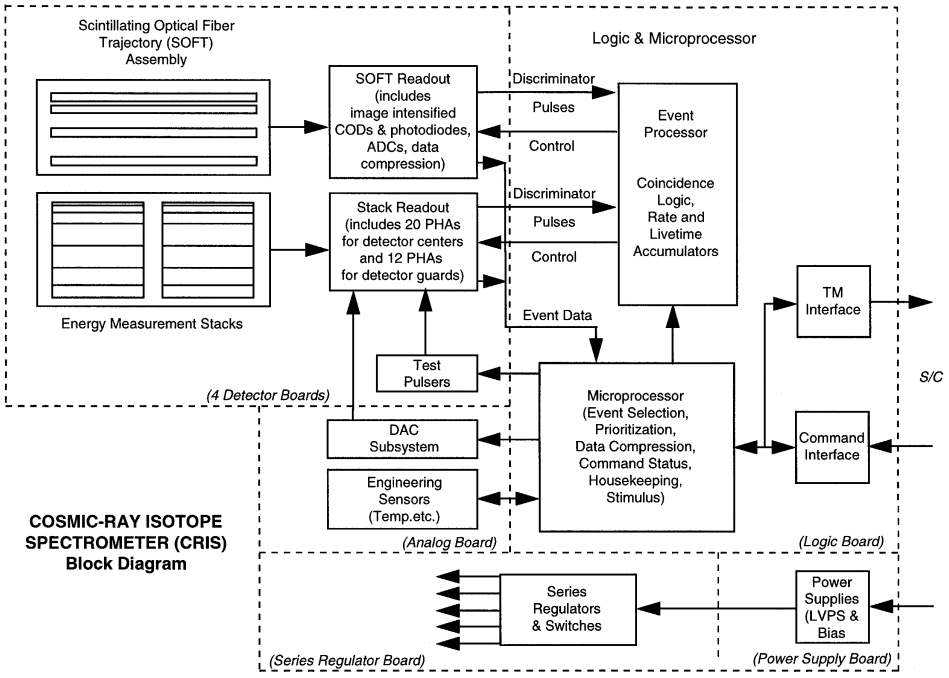

Figure 13. CRIS electronics block diagram.

5.1. LOGIC AND MICROPROCESSOR

As illustrated in Figure 13, the RTX2010 microprocessor forms the core of the system. The ease of programming and high performance level of this microprocessor influenced the hardware design from the outset, allowing simplification both of design and test. The microprocessor controls all other subsystems and also performs on-board data compression by analyzing the raw SOFT data to extract particle hit coordinates for each of the fiber layers. The main system logic and control functions were implemented as subsystems contained within Actel gate arrays which interface in a uniform way to the RTX2010 I/O bus. The logic and microprocessor system consumes less than 1 W and occupies only one single-sided printed circuit board measuring approximately 450 cm^2.

Although the capability of the RTX2010 was used to simplify hardware design, care was taken to perform the time-critical coincidence and pulse-height analysis control functions using a dedicated state machine referred to as the ‘event processor’. During front-end live time, the event processor loops waiting for a trigger formed by the logical OR of discriminator outputs associated with the 32 pulse-height analyzer hybrids used to read out the stack detectors and their guard rings. Any such trigger causes the event processor to leave the ‘live’ state and begin the coincidence determination sequence, which has two phases. At the end of the first phase, lasting approximately 4 μs, the status (triggered or not triggered) of

low level discriminators on the stack detector hybrids is latched. At the end of the second phase, lasting an additional 12 μs, the status of higher level discriminators for the stack detectors, as well as those from the SOFT trigger planes, is latched. Based on the latched data, event processing either proceeds to completion or is aborted to minimize dead time. Appendix B presents the boolean equations the CRIS logic uses to determine when a valid event has occurred.

The discriminators for the stack detector signals are set at various levels which allow an approximate sorting of events by nuclear charge. Low, medium, and high thresholds are triggered by stopping $Z \geq 1$, $Z \geq 2$, and $Z > 2$ particles, respectively, in a given detector. Thus, if only the low-level discriminators are triggered, an event receives a $Z = 1$ classification; if low and medium levels are exceeded but no high level, then $Z = 2$; and if any high level is exceeded, $Z > 2$. Processing of events classified as $Z = 1$ or $Z = 2$ may be terminated based on signals from the microprocessor which are used to throttle the rate of analysis of protons and He nuclei, ensuring adequate live time for the rarer heavy nuclei.

The CRIS electronic design provides a high degree of programmability. Discriminator thresholds and coincidence logic equations may be adjusted to compensate for noisy detectors or other anomalies. High voltage may be commanded off or on separately for various detector groups. All microprocessor code that is noncritical to communication with the spacecraft can be reprogrammed in flight.

Redundancy has been used selectively to increase reliability. Silicon detector high voltage is derived from four separate supplies. The A/B and C/D side front-end electronics are independent. The interface with the spacecraft is redundant. The SOFT system 0contains redundant camera systems, with separate interfaces to the main electronics.

5.2. STACK VLSI

0 Silicon detector wafers which form the four ‘stacks’ are grouped as discussed earlier to form 20 detector elements and 12 guard-ring elements. A separate pulse-height analyzer is used to read out each detector or guard element. These pulse-height analyzers and the associated stack-detector modules are mounted on four essentially identical printed circuit boards (‘detector boards’) housed below SOFT in the main card cage.

The pulse-height analyzers (PHAs) are hybrid circuits developed for ACE instruments during the project’s design phase and manufactured at Teledyne (Cook et al., 1993a). The only active component in the PHA hybrid is a fully custom bipolar application-specific integrated circuit (ASIC) fabricated at Harris Semiconductor. This new circuit represents an evolution of discrete bipolar transistor designs which were flight proven in numerous space instruments over the past thirty years (Halpern et al., 1968; Halpern and Marshall, 1968; Harrington and Marshall, 1968, 1969; Harrington et al., 1974; Althouse et al., 1978; Cook et al.,

1993b). The PHA hybrid has improved performance relative to the prior design, while using a factor of 10 less board area and a factor of 3 less power.

Each PHA hybrid includes a preamplifier, post amplifier, amplifier/offset gate (AOG), peak detector, and Wilkinson analog-to-digital converter (ADC). Shaping time constants are 2 μs, leading to a 3.0 μs time-to-peak for the bipolar signal. Twelve-bit digitization with a maximum conversion time of 256 μs is obtained with a 16-MHz clock. The PHA hybrid was manufactured in a number of types with preamplifier feedback and bias configured for different detector capacitances and leakage currents.

PHA hybrid performance surpasses design goals (see Table III), with typical dynamic range of 2000:1, gain stability of 20 ppm/°C, offset variation of less than 0.5 channels over -20 °C to $+40$ °C, and deviation from linearity of less than 0.01% of full scale over the entire dynamic range. Power consumption is 40 mW. The PHA hybrids do not contain the digital counters and logic needed for the Wilkinson ADCs, which are rather implemented in nearby Actel gate arrays.

Also mounted near the PHA hybrids are test pulsers used to simulate detector signals. There are two test pulsers per detector board, one for stimulating PHA hybrids connected to detector center elements and the other for guards. The center and guard test-pulse amplitudes are controlled by separate dual gain 8-bit DACs. The test pulsers allow thorough verification of the coincidence logic and are used in routine instrument functional checks. In flight, 'stim' events are continuously generated at a low rate to facilitate the monitoring of PHA stability.

The amplifier chains in the PHA hybrids are DC-coupled from the detector through the postamplifier. This eliminates the need for a long secondary AC coupling time constant and allows the DC level at the postamplifier output to be used to measure the detector leakage current. These measurements are incorporated into the instrument housekeeping data and are useful monitors of detector health.

5.3. SOFT CAMERA ELECTRONICS

Data acquisition and control for the SOFT cameras is provided by the camera electronics unit. These electronics provide the SOFT interface to the main CRIS electronics, control the CCD operation, manage the generation of high voltage and gating signals for the image intensifier, acquire, compress, and buffer the CCD data for transfer to the CRIS microprocessor, provide trigger pulses based on the photodiode signals, and condition the calibration LED light pulses.

The CCD is a 244×550 pixel array frame-transfer device. Light projected onto the CCD by the fiber reducer is integrated in the device's image zone. After the image has been acquired, the entire frame of data is clocked into an adjacent memory zone which is not exposed to incident light. The CCD employs an 'antiblooming' structure which greatly reduces electron spillover when the charge on a given pixel overflows its potential well. This antiblooming structure also allows a 'quick clear' to discard old information without the necessity of reading out the entire array.

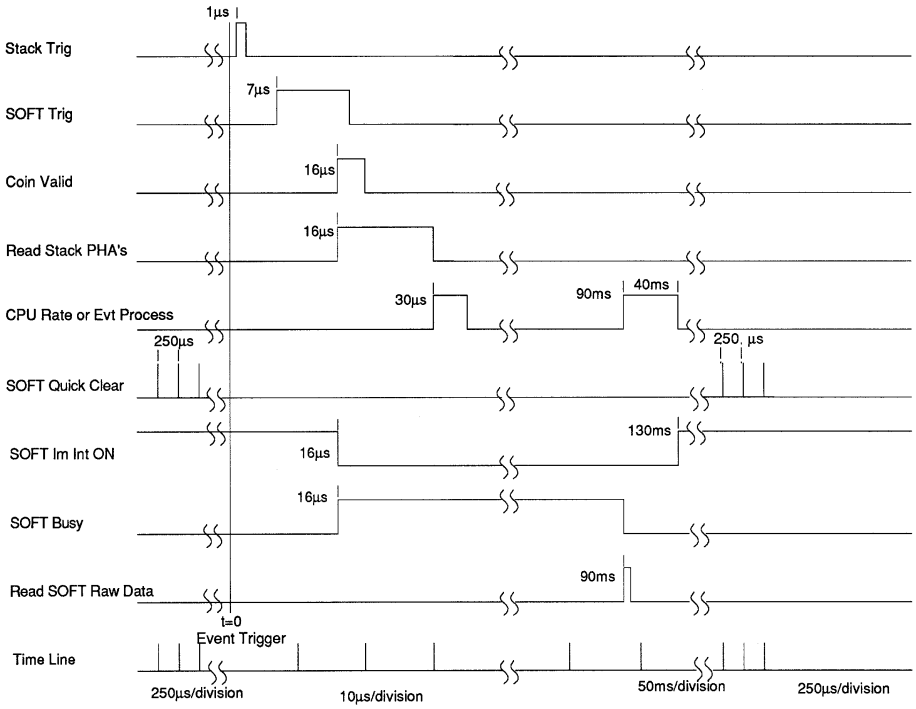

Figure 14. SOFT electronics timing diagram (see description in the text). Note that four different time scales are used, as indicated at the bottom of the figure.

Figure 14 shows the signal timing in normal operation. While waiting for an event, the camera electronics unit gates the image intensifier on and places the CCD in ‘integrate’ mode, i.e., data are not clocked out of the CCD. A quick clear is provided to the CCD to remove noise from the CCD image zone at a software selectable interval, typically every 192 μs. This reduces dark current build-up and minimizes background due to thermal electron emission at the cathode and to out-of-coincidence particles. When the CRIS silicon telescopes detect an event, a prompt trigger is sent to SOFT which inhibits quick clears and begins a 1.5 ms integration of the CCD (not shown). Approximately 7 μs after the prompt trigger the SOFT photodiodes provide discriminator pulses to the CRIS logic for event validation if they have also seen a signal. Events which fail the event coincidence criteria result in a camera reset and quick clears resume. If the event is valid, the 1.5 ms integration proceeds, after which the information in the image zone is transferred to the CCD memory zone in 496 μs. The pixel data from the CCD are clocked at 2.0 MHz through an analog discriminator. When a pixel is encountered which is above threshold, the clocking rate is slowed to 100 kHz and the pixel signal is passed to a 12-bit ADC. This fast/slow clocking provides a large dynamic range while minimizing the overall readout time, typically 90–300 ms.

For each CCD pixel row which has data above threshold, a row header and address are inserted into the data stream that goes into the SOFT memory. A column header and address are then inserted ahead of each contiguous segment of pixels above threshold. After an event has been read out and stored in the SOFT camera memory it is transferred to the CRIS microprocessor for compression and merging with the stack data (see Section 5.4.1).

5.4. CRIS DATA

The data returned by the CRIS instrument consist predominantly of 'events', each containing the pulse-height and trajectory measurements for a single detected nucleus. The microprocessor categorizes the events to assign priorities and optimize the mix of events that can be telemetered within the CRIS bit rate allocation. In addition, a small fraction of the data stream is used for housekeeping measurements and rates. These quantities are multiplexed over a 256-s 'instrument cycle'. Finally, when commands are sent to the instrument a command echo/command reply is inserted into the data stream. The following subsections describe each of these components of the CRIS data.

5.4.1. *Event Data*

A valid particle event in CRIS must produce a signal in the SOFT trigger plane, penetrate a certain minimum distance into the silicon-detector stack (typically at least to E2, although a greater depth requirement could be set by command), and generally not trigger the guard rings around the silicon-detector stack. For each such event, the CRIS microprocessor reads a 12-bit pulse height from all of the silicon-detector PHAs that had signals above their low-level discriminator threshold and video data from the SOFT electronics. The raw SOFT data consist of the location and intensity of every pixel above a commandable threshold intensity in whichever of the two SOFT CCD cameras is active at the time.

To maximize the number of events sent to the ground in the 464 bits-per-second telemetry rate allocated to CRIS, these event data are compressed on-board. Most importantly, the pixel data from the SOFT camera are processed to identify pixel 'clusters' (contiguous groups of pixels that meet cluster criteria set by several commandable parameters) which can be represented by a pair of centroid coordinates and an intensity. The centroids are recorded in 'half-pixel' increments for both x and y. Normal operation calls for recording the two brightest clusters in each of the fiber layers plus an additional six clusters (if they are present) for an overall maximum of 18 clusters per event. These numbers are adjustable in flight, if circumstances warrant.

In addition to data compression through the on-board extraction of SOFT centroids, further reduction is achieved by using a variable-length data format in which the event size is adjusted to match the number of sensor signals that are present. Details of the format are discussed in Appendix C.

As a result of this format, the lengths of CRIS events may vary considerably, ranging from a minimum of around 31 bytes for particles stopping in E2 in only one telescope while triggering no guards and producing six SOFT clusters, to an extreme maximum of 162 bytes for a pulser-stimulated event triggering all stack detectors and guards in both telescope pairs, with 31 SOFT clusters. A 'typical' event stopping in E4 of only one telescope, with no guards and 12 SOFT clusters is 52 bytes long.

In addition to these compressed, normal-mode events, 'diagnostic-mode' events are also sent back at a low, commandable rate (typically about one every few hours). Such an event consists of the pulse-height data from all 32 silicon stack and guard PHAs, the associated discriminator tag bits, and the position and intensity of each triggered SOFT pixel, rather than just clusters of adjacent pixels. Included with these raw data is the compressed, normal mode interpretation of the event. Such diagnostic events allow potential problems in the on-board compression algorithms to be identified so that they may be fixed by adjusting parameters in the algorithms by command. These events may be very large, up to about 6000 bytes.

5.4.2. *Priority System*

It takes the instrument about 130 ms to process a typical event (limited primarily by the SOFT system), allowing $\sim$ 7 to 8 events per second to be processed. Given the average event lengths and the CRIS telemetry allocation of 58 bytes per second (which also includes count rate and housekeeping data), only about 1 event per second can be telemetered. Actual event rates for stopping particles with $Z > 2$ are expected to be only about 0.1 to 0.2 events per second during solar quiet times, but penetrating particles, protons, and alpha particles can increase the trigger rate to several per second. In order to maximize the return of the more interesting stopping, heavy-ion events, the CRIS microprocessor sorts the events into 61 different buffers on the basis of range, pulse height (which indicates particle species), quality of trajectory measurements, single or multiple telescope hits, and potential pulse pile-up, or 'hazard', condition. Events are read out from the buffers in a commandable order, with the highest priority going to events with long ranges, high Z, good trajectory measurements, and single telescope, non-hazard stack pulse heights. Appendix D presents the definitions of the CRIS event buffers, and the priorities that were assigned to them at launch.

Also, a commandable number of events (nominally 10) in each 256-s instrument cycle are read out using a simple polling scheme, sequentially reading from each of the buffers in turn. This ensures a more uniform sample of all event types and prevents the possibility of the lowest priority events being eliminated entirely during periods of higher particle intensity. The event buffers are 512 bytes in size, and can contain approximately 10 events.

5.4.3. *Rate and Housekeeping Data*

In addition to pulse-height data, CRIS records and transmits a number of count rates:

– 'singles' count rate data for each of the two SOFT hodoscope trigger signals and each of the 32 silicon stack and guard PHAs,

– 15 different coincidence rates,

– various diagnostic rates useful for monitoring the event processing,

– three separate live times corresponding to the $Z = 1$, $Z = 2$, and $Z > 2$ classifications (see Section 5.1),

– rates from each of the 61 event buffers, which are needed to calculate sampling efficiencies and thus obtain absolute fluxes for each category of events.

All rates are read out during each 256-s instrument cycle. Any two of these rates may be selected as 'high-priority' rates to be read and transmitted at a higher time resolution of once every 16 s.

A number of housekeeping measurements are also recorded, including temperatures, voltage and current monitors for the low- and high-voltage power supplies, and silicon-detector leakage currents (derived from the DC outputs of the PHA hybrids). In the remaining telemetry space, the CRIS command table (844 bytes) is slowly trickled out, taking 13 instrument cycles ($\sim$56 min) to transmit the entire table.

5.4.4. *Telemetry Format*

The above data are packaged into a 58-byte-long CRIS instrument minor frame*. The first bit of the instrument frame is used to find the start of the 256 minor frame instrument cycle, which need not coincide with the start of a spacecraft major frame. It is set to 0 for the first 128 minor frames, and 1 for the next 128 frames of the cycle. The second bit serves as a flag to indicate that a command response precedes the event data in this minor frame. All commands are echoed back in the CRIS telemetry data, along with any output generated by the command, thus documenting the command history of the instrument within the data stream. Command responses vary in length up to 55 bytes. The first byte of a command response gives the length of the remainder of the command echo. The rest of the minor frame not used by the command response contains normal mode or diagnostic-mode data. The third bit of the instrument frame is set if the pulse-height data in this frame are from a diagnostic-mode event rather than a normal, compressed event. Diagnostic events may span any number of contiguous minor frames, and may start in the middle of a normal event (which then continues after the end of the diagnostic event). After the first three bits of the instrument frame, the remaining 21 bits in the first three bytes are allocated to rate and housekeeping data. All rates are 21

* The start of the CRIS 'instrument frame' is offset by four bytes from the beginning of the CRIS data block in the ACE spacecraft minor frame to simplify data handling by the microprocessor.

bit numbers† and each is assigned to a particular frame in the instrument cycle. Housekeeping data are typically 10 bit quantities, and are packaged 2 per frame, for those frames in which they appear. Those frames where the housekeeping/rate data consist of part of the command table readout contain two bytes of the command table.

The rest of the instrument frame after the first three bytes is filled out with command responses and/or event data (either normal or diagnostic), as indicated by the second and third bits of the frame. Events can span the boundary from one frame to the next, and are strung sequentially together to maximize the use of telemetry space. Only at the beginning of the 256-s instrument cycle is an event forced to start at the beginning of the event data section of the frame. The event format (see Appendix C) contains enough redundant information to allow identification of the start of an event, thereby making it possible to regain synchronization should telemetry frames be dropped within an instrument cycle.

5.5. CRIS COMMANDS

Commanding of the CRIS instrument is accomplished using strings of ASCII characters which are passed to the command interpreter of the Forth operating system running on the RTX2010 microprocessor. As such the command system has almost arbitrary flexibility to alter the operation of the instrument. In practice, most commanding is done by altering entries in a 'command table' which holds the present values of a large number of instrument parameters. Table VII summarizes the major categories of CRIS operating parameters that are set by command.

In addition, large blocks of code can be uploaded into the microprocessor's memory to alter its programming. This function is not used in normal operation, but does allow the possibility of major reprogramming should that become necessary.

6. Mechanical Design and Packaging

The mechanical design of CRIS provides the following features:

- Precise and reproducible mechanical positioning of detectors.
- Minimal use of wires and coaxial cables for interconnections.
- Close proximity of detectors to their preamplifiers with short interconnections.
- RF shielding of the detectors.
- Ease of assembly and component replacement.
- Light-tight enclosure of detectors which can vent rapidly at launch.
- Dry nitrogen purge to detectors until just prior to launch.

† A few of the rates which could attain large values, particularly those associated with the SOFT trigger signals, are prescaled by a factor of 32 when they exceed a value of 2^{20}. Otherwise the rates are uncompressed.

TABLE VII
CRIS command summary

Item	Comments
Coincidence logic	
Coincidence equation	Set minimum range for coincidence
Hazard event	Allow/disallow analysis of hazard events
Stim event	Give stim events highest priority
ADC2 definition	Allow/disallow trigger on any two successive detectors in stack
Stack operation	
Connect/disconnect bias	Separate switch for each detector set
Adjust ADC thresholds	Raise/lower in steps of ∼10%
PHA operation	Individually enable/disable any PHA
Medium/high PHA thresholds	Raise/lower in steps of 10%
H and He event timers[a]	Individually adjust from 0 to 130 s
Hodoscope operation	
Active camera	Select A or B camera
MCP quick clear	Adjust period from 32 to 512 μs
LED stim pulse	Adjust length from 0.25 to 16 μs
CCD high voltage	Adjust from 0 to 2050 V (camera A) or 2200 V (camera B)
Trigger discriminator level	Adjust from 0 to 25% of full scale
Pixel discriminator level	Adjust from 0 to 5.6% of full scale
Cluster parameters	Set cluster criteria and limits
Software parameters	
Charge buffers	Adjust boundaries
Readout priority system	Redefine event buffer readout priorities
Event format	Enable/disable transmission of guard pulse heights, 2nd telescope data
High priority rates	Select 2 rates for 16 s accumulation
Stim events	Select period and PHAs to be pulsed
Diagnostic events	Select period

[a]Timers are used to artificially create additional dead time for H and He events to throttle the rate of analysis of these lower priority events.

The SOFT trajectory system was the primary responsibility of Washington University at St. Louis, whereas the remainder of CRIS was primarily the responsibility of Caltech. This made a modular design approach particularly desirable. Thus CRIS is housed in two boxes (Figure 7) attached to one another with simple mechanical and electrical interfaces. The upper box houses the SOFT hodoscope and the lower box contains the remainder of CRIS. The lower box contains in-

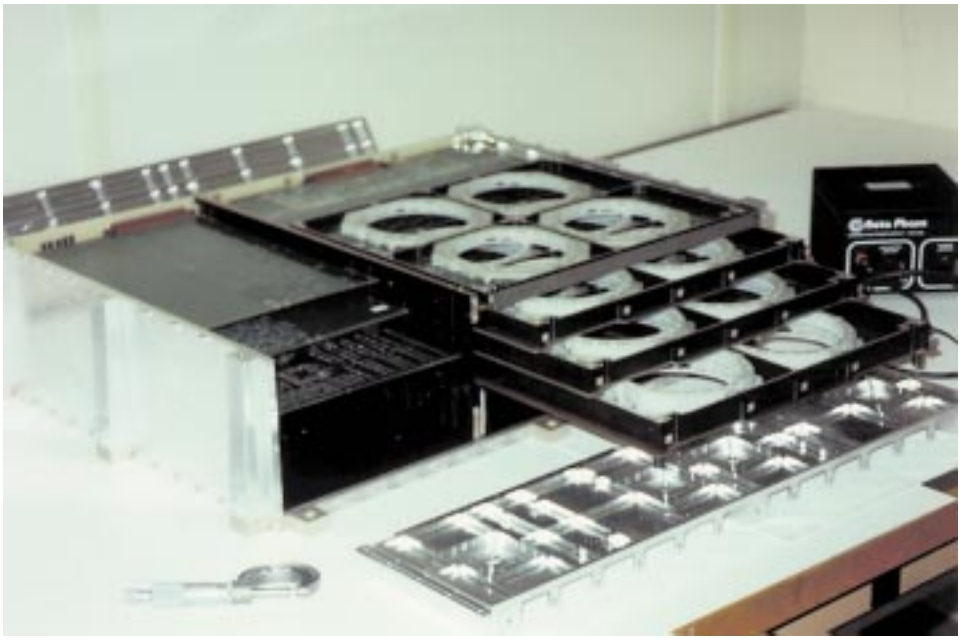

Figure 15. Mounting of the CRIS detector boards in the main CRIS box. Detectors and their front-end electronics are mounted on four boards (E1/E2, E3/E4, E5/E6, and E7/E8/E9) which slide into a card cage/backplane housing. For this photograph, the detector boards were only partially inserted to illustrate the assembly approach.

dividual printed-circuit boards (PCBs) which slide into card rails and mate with zero-insertion-force (ZIF) connectors mounted on a PCB backplane at the rear of the box as shown in Figure 15. The card rails then lock the PCBs to the walls of the box using jackscrews accessible from the ends of the card rails after the boards are in place. The ZIF connectors (made by Betaphase Corporation, Inc.) on the motherboard backplane provide connections on each side of each daughter board on 0.635 mm centers (80 per inch). The Betaphase connectors are operated by applying a voltage to an internal heater which causes the jaws of the connector to open and allows the board to slide into a keyed slot. Electrical connections are made as the connector cools and clamps the board, gripping it with substantial force.

Some of the printed-circuit boards carry only electronic components, while others include module housings containing multiple detectors. The four stacks of solid-state detectors below SOFT are each formed by four vertical sets of such detector modules, one above the other. An example of a detector module is shown in Figure 16 and a sample CRIS printed-circuit board carrying four modules is shown in Figure 17. Note from Figure 17 that each module is surrounded by an aluminum ‘fence’ which provides an RF shield around the module.

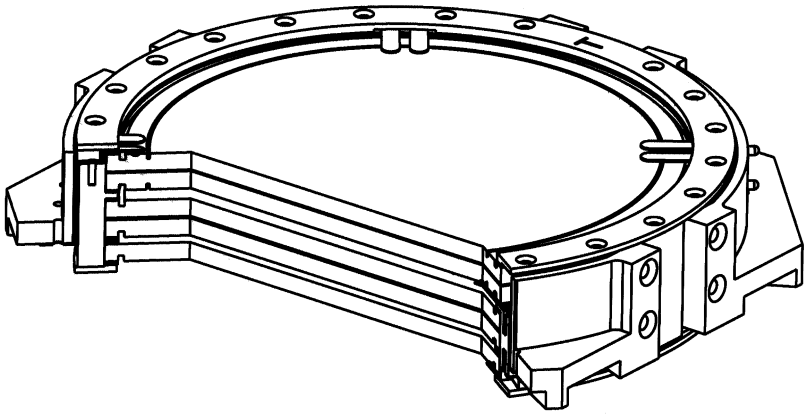

Figure 16. Cut-away drawing of a CRIS detector module (E7/E8/E9) with detectors installed. The module is machined from G10, which has a thermal coefficient of expansion well matched to that of the silicon. Electrical contacts to the center and guard ring are made with BeCu spring contacts. The detectors housed in this module are, from top to bottom, E7-1, E7-2, E8-1, E8-2, and E9. Note that for the detector pairs which are connected in parallel to a single PHA (such as E7-1 and E7-2) the ungrooved surfaces face one another, eliminating significant dead layers midway through the two-detector combination.

Connections in a module are made to each Si(Li) detector using gold-coated dimples on spring-loaded (BeCu) fingers. These fingers make pressure contact with the detector surface and then run internal to the module to fingers which make pressure contact with traces on the printed-circuit board. In the case of double-grooved detectors, separate contacts are made to the detector central areas and to the detector guard rings. Detector modules can be easily installed or removed from their respective printed-circuit boards and detectors can also be installed or removed from their module housings with relative ease.

The isotopic resolution criteria put limits on acceptable position tolerances. The allowable mechanical tolerances used in designing the CRIS instrument are listed in Table III. These levels of alignment were achieved by minimizing the stack-up of parts, which in turn keeps the tolerance accumulation to a minimum. Feet on the bottom of each RF shield extend through the printed-circuit board and mate to the top of the RF shield on the module below. This prevents build-up of position errors that otherwise might result due to the fact that the multi-layer printed-circuit board thicknesses are relatively difficult to control. After all the CRIS boards are installed (but before the card rails are tightened), five alignment bolts are inserted from the bottom of the CRIS box, extending from the bottom plate up through all the RF shields except the topmost one, and screwed into the top shield. These bolts are intended primarily to align the modules in a reproducible way. The RF shielding around each module is not perfect, since there typically remains a gap of $\sim$0.1 mm between each shield and the board above it.

Figure 17. Photograph of a CRIS detector board with all parts installed. The four detectors are surrounded by conducting 'fences' which serve as RF shielding and have precisely machined heights that permit stacking of successive detector boards with minimal build-up of tolerances. Immediately to the right of the detectors are eight hybrid pulse-height analyzers: on this board they process signals from E3AB, E4AB, E3CD, E4CD, G3AB, G4AB, G3CD, and G4CD.

CRIS has a system of purge tubes which allows dry nitrogen gas to be piped through the RF shielding system and directly into the modules where the detectors reside. Vent ports in the side walls of both SOFT and the lower CRIS box were designed to allow rapid evacuation of the boxes during launch. Baffles on the vent ports block light from entering through the instrument walls.

Apart from a front window of 254 μm (0.010″) aluminum and a thermal blanket (0.083 g cm^{-2}), the primary field of view of CRIS (45° half angle*) is completely unobstructed. The bottom of the SOFT box is a 127 μm (0.005″) aluminum sheet which isolates the two boxes while introducing only a small thickness of material into the paths of the detected particles.

CRIS is mounted on a side wall of the spacecraft with its average view direction perpendicular to the spin axis. The instrument is covered with thermal blankets on all sides except the side facing furthest away from the Sun, which is covered with

* The CRIS field of view is a complicated function of location on the detectors and azimuthal angle.

silver teflon and acts as a radiator to remove heat from the instrument. Each SOFT image intensifier also has an uncovered radiative cooler surface (see Figure 7).

Accelerometers are mounted between CRIS and the spacecraft on all 12 CRIS mounting feet. These provide signals to the Structural Loads and Acoustics Measurements (SLAM) instrument* which is designed to record the vibration environment during launch. These data should aid in setting more realistic vibration test specifications for future missions.

7. Resource Utilization

The CRIS instrument is composed of two rectangular boxes of slightly different dimensions which are joined together. The top box houses the SOFT system and has dimensions ($l \times w \times h$) of 53.3 cm × 43.8 cm × 10.1 cm. The bottom box contains the stack detectors and most of the electronics and has dimensions 53.3 cm × 40.6 cm × 13.4 cm. CRIS has a mass of 29.2 kg, which does not include mounting hardware, force transducers, or thermal blankets. The thermal blankets have a mass of 1.0 kg.

Under normal operating conditions, CRIS dissipates ∼12 W of power. However, the power consumption depends on temperature and activity level. During high rate periods at the highest temperature for which the detectors are rated (35 °C), the power is expected to rise to ∼16 W. Much of this increase is due to the large temperature coefficient of the leakage current of the Si(Li) detectors (factor ∼2 per 7 °C).

Operational heaters of 1.7 W are mounted on each image intensifier; another operational heater of 4.2 W is mounted on the backplane. Survival heaters of 1.6 W are mounted on each image intensifier; another survival heater of 15.4 W is on the outside of CRIS under the thermal blanket. The CRIS mounting bolts are thermally isolated from CRIS via Ultem bushings. The nominal internal operating temperature for CRIS is approximately −10 °C.

8. Expected Performance

In order to confirm that the CRIS instrument design would be suitable for meeting the requirements discussed in Section 3.2, a variety of calculations of the expected performance were carried out. The results of these calculations are discussed in the following subsections.

* The SLAM instrument was developed at the NASA/Goddard Space Flight Center under the direction of Scott Milne and Ken Hinkle.

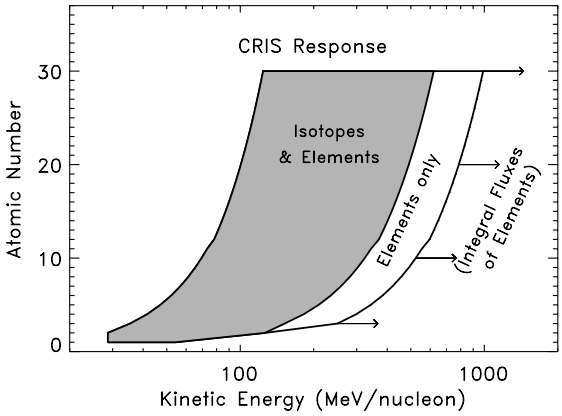

Figure 18. Energy intervals covered by the CRIS instrument as a function of the atomic number, Z, of the detected nucleus. Isotope measurements are made for particles that stop in the silicon-detector telescopes. When the particles penetrate the entire telescope but still slow significantly, charge and energy identification is still possible, but not mass determination. At the highest energies, major elements can be identified, but only lower limits can be set on their energies.

8.1. Energy Coverage versus Atomic Number

Figure 18 shows, for the range of atomic numbers observed by CRIS, the calculated energy intervals over which the instrument can identify isotopes and elements. The most precise particle identification is achieved in the shaded region, defined by the requirement that nuclei stop in one of the silicon-detector stacks between E2 and E8. In this region CRIS will make a precise measurement of each particle's total energy, as well as one or more measurements of $\mathrm{d}E/\mathrm{d}x$. From these quantities and the particle trajectories, both the charge and the mass of each detected nucleus can be derived.

In the region labeled 'Elements only' particles will penetrate the entire stack and their total energies will not be directly measured. However, these nuclei undergo significant slowing in the silicon-detector stack, resulting in measurable increases in $\mathrm{d}E/\mathrm{d}x$ going from the front to the back detectors in the stack. From these patterns of $\mathrm{d}E/\mathrm{d}x$ values (the Bragg curves) one can calculate the atomic number and kinetic energy of each particle. The total energy estimates are not, however, sufficiently accurate to permit reliable derivation of particle masses.

In the right-most region of the plot the particles are so energetic that their velocities do not change significantly in the stack, so it is only possible to set a lower limit on each particle's energy. However, since at high energies $\mathrm{d}E/\mathrm{d}x \propto Z^2$ with relatively little energy dependence, it is possible to estimate the charge. Thus for the more abundant elements it may be possible to use the measurements in this high-energy region to derive integral flux values*.

* The high-energy data set will include particles which pass through CRIS in the backwards direction, after having traversed a significant amount of material in the spacecraft. It remains to

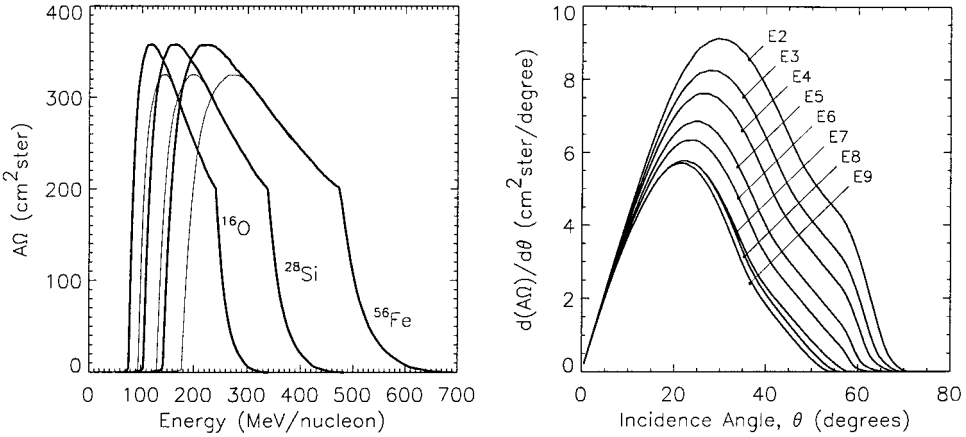

Figure 19. CRIS geometrical factor ($A\Omega$). The left panel shows the geometrical factor as a function of particle energy for ^{16}O, ^{28}Si, and ^{56}Fe nuclei. The heavy curves indicate the geometrical factors including particles which stop anywhere between E2 and E8, inclusive. When redundant dE/dx measurements are required, the particles must penetrate to at least E3. In this case the geometrical factors are reduced to the values shown with the light curves. The right panel shows the geometrical factor per unit incidence angle (θ) for particles stopping in each detector, as a function of θ. The curve labeled 'E9' also gives the geometrical factor for nuclei which penetrate the entire telescope. In both panels the ordinate values include the responses of all four CRIS telescopes.

The elements hydrogen and helium are not included among the primary objectives of CRIS: the SOFT efficiency for these species is relatively low, and at high energies they fall below threshold in the stack detectors. Nevertheless, over a limited energy interval CRIS will provide measurements of these light elements that can be used to relate the fluxes of the heavy nuclei which are the primary CRIS objectives to those of H and He, which constitute the bulk of the cosmic rays.

8.2. ANTICIPATED NUMBERS OF PARTICLES

Figure 19 shows the results of Monte Carlo calculations of the CRIS geometrical factor, $A\Omega$. In the left panel $A\Omega$ is plotted as a function of particle energy for the elements O, Si, and Fe. The right panel shows the differential geometrical factor per-unit incidence angle, d$A\Omega$/dθ, as a function of θ and of the detector in which the particle stops. The CRIS response extends to large angles, $>60°$, because of the large active area provided by the SOFT hodoscope. The curve labeled 'E9' also gives the geometrical factor distribution for penetrating particles exiting through the back of the CRIS telescopes.

Figure 20 shows the number of good events expected from CRIS for each stable or long lived nuclide with $3 \leq Z \leq 30$. This calculation assumes data collection over a period of two years under solar minimum conditions. It takes into account

be determined whether useful integral flux measurements can be derived in the presence of this background.

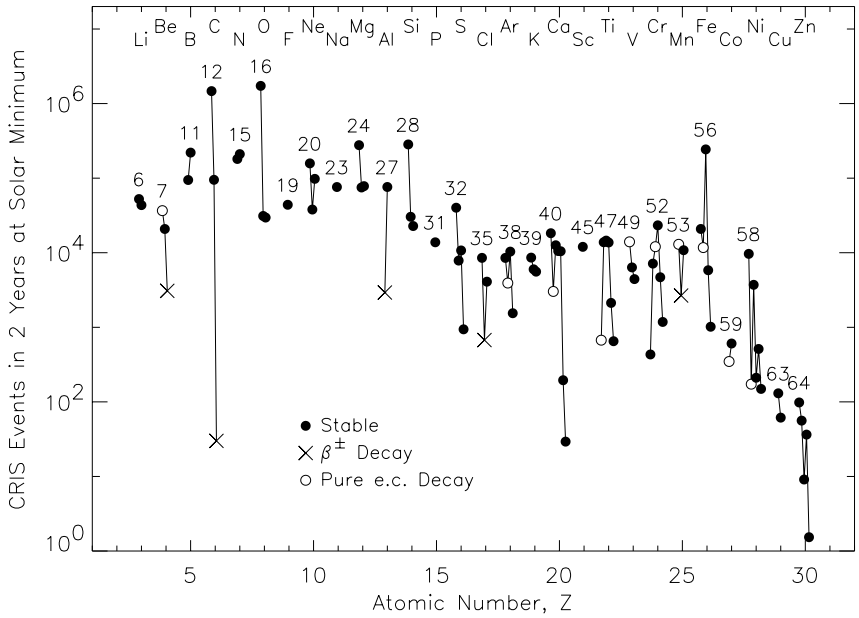

Figure 20. Number of good events expected for each isotope with two years of data collection at solar minimum. Only particles which have incidence angles $<45°$ and which come to rest in the Si(Li) detector stacks without fragmenting are included. It is assumed that isotopes that can only decay by electron capture are effectively stable in the cosmic rays.

the geometrical factor distributions shown in Figure 19 and the energy intervals set by the thicknesses of the CRIS detectors. Particles which fragment in the instrument have been excluded, as have nuclei with angles of incidence $>45°$ since at the largest angles the mass resolution degrades due to effects such as multiple Coulomb scattering (see Appendix A). This plot includes all particles which stop between E2 and E8, inclusive. For those which stop in E3 or beyond, one has two or more mass determinations which can be compared to remove background events. However, for particles which stop in E2, one has only a single mass determination and cannot test the energy loss data for internal consistency. Consequently, the E2-stopping events are subject to more background contamination than higher energy events. For the rarest species this extra background may degrade the quality of the abundance measurements. For such nuclides it may be desirable to restrict the analysis to those particles which stop in E3 or beyond. In this case the event yields are reduced by $\sim$15%, as suggested by Figure 19.

In addition to accurately measuring abundances of rare nuclei, CRIS will also collect large samples of the more abundant isotopes over short time intervals. These measurements will allow studies of spectral changes over times as short as a solar rotation, thereby enabling detailed studies of the solar modulation of galactic cosmic rays.

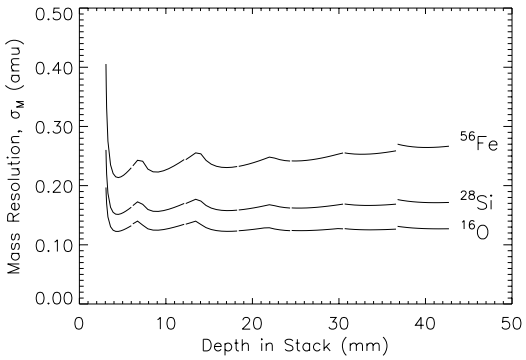

Figure 21. Calculated mass resolution for ^{16}O, ^{28}Si, and ^{56}Fe is shown as a function of the depth to which the particles penetrate in the CRIS silicon-detector stacks. The calculations were performed for an incidence angle $\theta = 20°$. The mass resolution is calculated with various combinations of detectors summed to form ΔE and E', with the best combination selected at each penetration depth. Discontinuities occur at depths where the detector combinations used for the ΔE and E' measurements are changed. The abrupt increase in the mass resolution at the front of the stack (just entering E2) is due to a large path length uncertainty due to multiple scattering for these particles which almost come to rest in E1.

8.3. EXPECTED MASS RESOLUTION

The expected mass resolution was evaluated using the formulas discussed in Appendix A and taking into account the measured characteristics of the CRIS instrument. Figure 21 shows the results of these calculations for the isotopes ^{16}O, ^{28}Si, and ^{56}Fe as a function of the depth to which the particles penetrate in the silicon-detector telescopes. For these calculations, an angle of incidence $\theta = 20°$ has been used. The overall mass resolution is dominated by a combination of Bohr/Landau fluctuations and multiple scattering in the ΔE detectors. Contributions to the mass resolution from uncertainties in the measurements of trajectories and energy losses are small compared to these fundamental contributions, as intended. The mass resolution has a significant dependence on the angle of incidence, with better resolution at smaller angles. This dependence can be used to select higher resolution data sets, when needed, at the expense of reduced statistical accuracy.

9. Accelerator Calibrations

Accelerator tests and calibrations played an important role in the development of the CRIS instrument. Prototypes of both the SOFT hodoscope and of the Si(Li) detectors were tested in a sequence of runs at the Michigan State University National Superconducting Cyclotron Laboratory (MSU/NSCL) in order to optimize the designs and to demonstrate that the performance of these sensors was sufficient to meet the CRIS requirements.

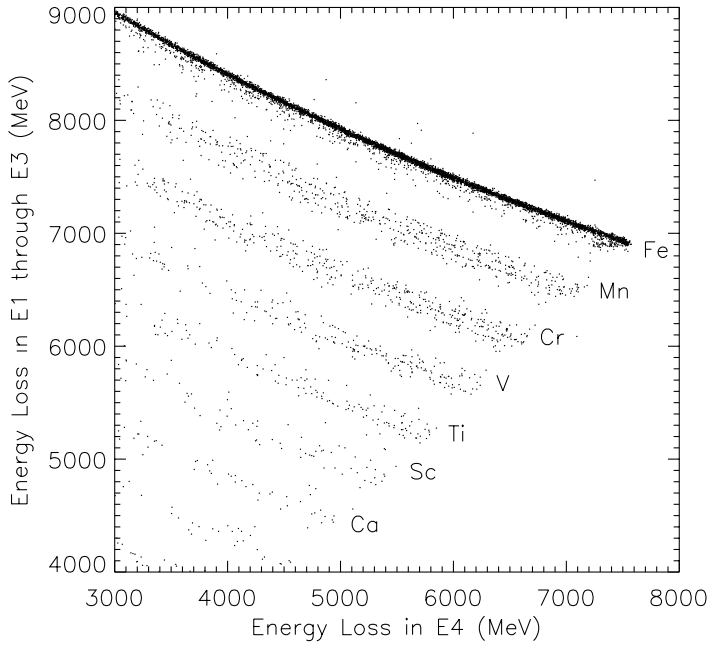

Figure 22. ΔE vs E' scatter plot from a GSI calibration run. A primary beam of ^{56}Fe nuclei was incident on a target in which a portion of the nuclei fragmented, producing lighter nuclides. 'Energy degraders' were used to distribute the stopping particles throughout the entire thickness of a CRIS stack. The nuclei had a nominal angle of incidence of 10°.

The thicknesses and dead layers of the Si(Li) detectors were mapped in detail at the MSU/NSCL, as discussed in Section 4.2.3. In other runs, the correspondence between SOFT pixel centroids and absolute positions was calibrated (Section 9.2) and the SOFT efficiencies were derived (Section 9.4).

The completed CRIS instrument was calibrated at the GSI accelerator in Darmstadt, Germany, since this facility is capable of providing beams of heavy nuclei sufficiently energetic to penetrate the entire thickness of the CRIS telescopes. These measurements provide the best pre-launch checks of the overall instrument performance.

9.1. MEASURED MASS RESOLUTION

Figure 22 shows a scatter plot from a GSI calibration run in which a beam of ^{56}Fe at 500 MeV nucl^{-1} was fragmented in a polyethylene target and was spread in energy before impinging on CRIS at an angle of 10°. This plot shows well-resolved tracks for the primary ^{56}Fe and a variety of fragment nuclei. Using these data, the charge and mass of each detected nucleus was calculated using Equation (1) (Section 3.1) and taking into account the measured gains and offsets of the pulse-height analyzers and the calibrated mean thicknesses and dead layers of the penetrated detectors

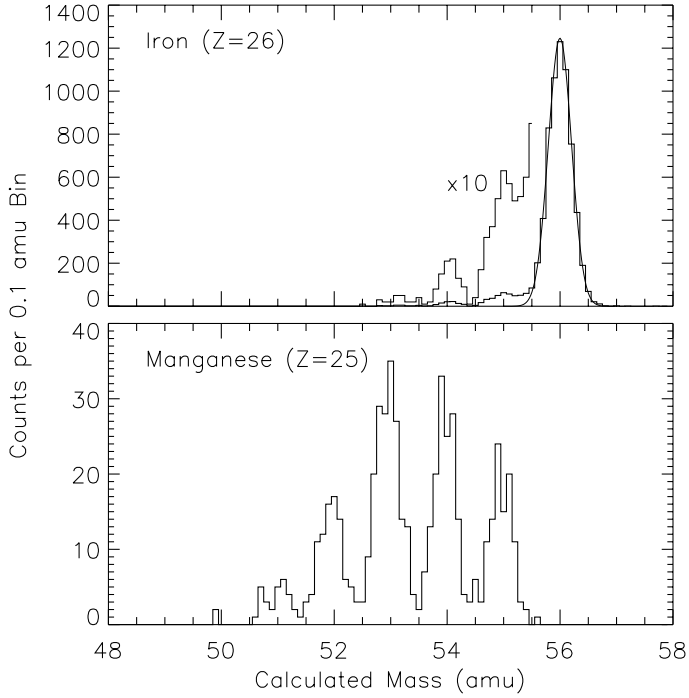

Figure 23. Mass histograms of CRIS accelerator calibration data derived from the measurements of ΔE and E' shown in Figure 22. In this analysis, no corrections were made either for the deviation of the angle from the nominal value (10°), or for the spatial variation of the detector thickness (although the beam area was small enough so that mapping corrections should be insignificant). The histograms show events stopping in E4, with masses calculated using the sum of the energy losses in E1, E2, and E3 as ΔE, and the signal from E4 as E'. The smooth curve in the iron histogram is the result of fitting the ^{56}Fe peak with a Gaussian, resulting in $\sigma_M = 0.205$ amu. The region of the measured iron distribution below 55.5 amu is shown expanded (light line) to illustrate the separation between ^{56}Fe and the lighter isotopes, which have lower abundances by a factor $\gtrsim$20 in this run.

(but not yet using detailed thickness maps). Figure 23 shows the resulting mass histograms for Fe and Mn and indicates the instrument's capability for identifying isotopes up through the iron group.

Calibrations of this type were carried out using a variety of primary beam particles, energies, and incidence angles. Generally, it was found that the CRIS mass resolution ranges from ∼0.25 to ∼0.30 amu for iron-group elements down to ∼0.1 amu for the lightest nuclei of interest. The mass resolution increases somewhat at the lowest energies and the largest angles measured in CRIS.

9.2. SOFT COORDINATE CALIBRATION

The data required to convert pixel centroids measured in the SOFT cameras into calibrated spatial coordinates were obtained using an oxygen beam from the MSU/NSCL cyclotron. This calibration was carried out in two stages: first the

correspondence between the location on the CCD pixel array and the number of the hit fiber was mapped, then the relationship between xy fiber pairs and specific fiducial points in space was measured.

Figure 24 shows a superposition in CCD pixel space of centroids obtained when the full area of SOFT was scanned with the oxygen beam. The centroids cluster around locations corresponding to the fiber centers. Fitting the mean xy pixel location for each fiber in the array and partitioning the pixel space into cells centered on each fiber yields the necessary pixel-to-fiber calibration.

The identity of the hit fibers provide initial estimates of the spatial coordinates, good to $\lesssim 1$ mm. An additional mapping step was carried out to correct for small imperfections in the straightness and spacing of the fibers. For this purpose the SOFT hodoscope was exposed to the oxygen beam through a plate having holes machined on a regular grid. As shown in Figure 25, the data from this run produced images of the fiducial holes which established the correspondence between fiber numbers and spatial coordinates. In using this map to derive coordinates for detected particles, pairs of fiber numbers (one x fiber and one y fiber) are converted to two-dimensional spatial locations, thereby taking into account any deviations of the fibers from straightness. While this adds to the complexity of the SOFT data analysis (since there are generally a number of different possible pairings of a given set of individual coordinates), it is important for fully optimizing the spatial resolution.

9.3. Position and angular resolution

The SOFT detector position resolution was evaluated using the method of residuals (Crary et al., 1992; Davis et al., 1989). Cluster centroids were derived from the CCD images using an algorithm similar to that employed on board CRIS, and these were converted to spatial coordinates using the mapping procedures discussed above. Distributions were then made of the differences (ΔX2 and ΔY2) between the coordinates obtained for the H2 plane and the coordinates expected at that location based on a straight line track derived from the coordinates in the H1 and H3 planes.

Figure 26 shows one such distribution obtained from a full-area exposure of the detector using 155 MeV nucl^{-1} oxygen nuclei with an incidence angle of 0°. The measured standard deviation, 102 μm, implies a single-coordinate spatial resolution of 83 μm (Crary et al., 1992), assuming comparable resolutions for all SOFT layers. From SOFT measurements with this resolution the angle of incidence of detected nuclei can be derived with an accuracy $\lesssim 0.1°$.

Figure 27 shows the dependence of spatial resolution on the energy deposited in SOFT. These measurements demonstrate that the SOFT hodoscope is achieving the required trajectory resolution for all elements to be studied with CRIS (see Table III).

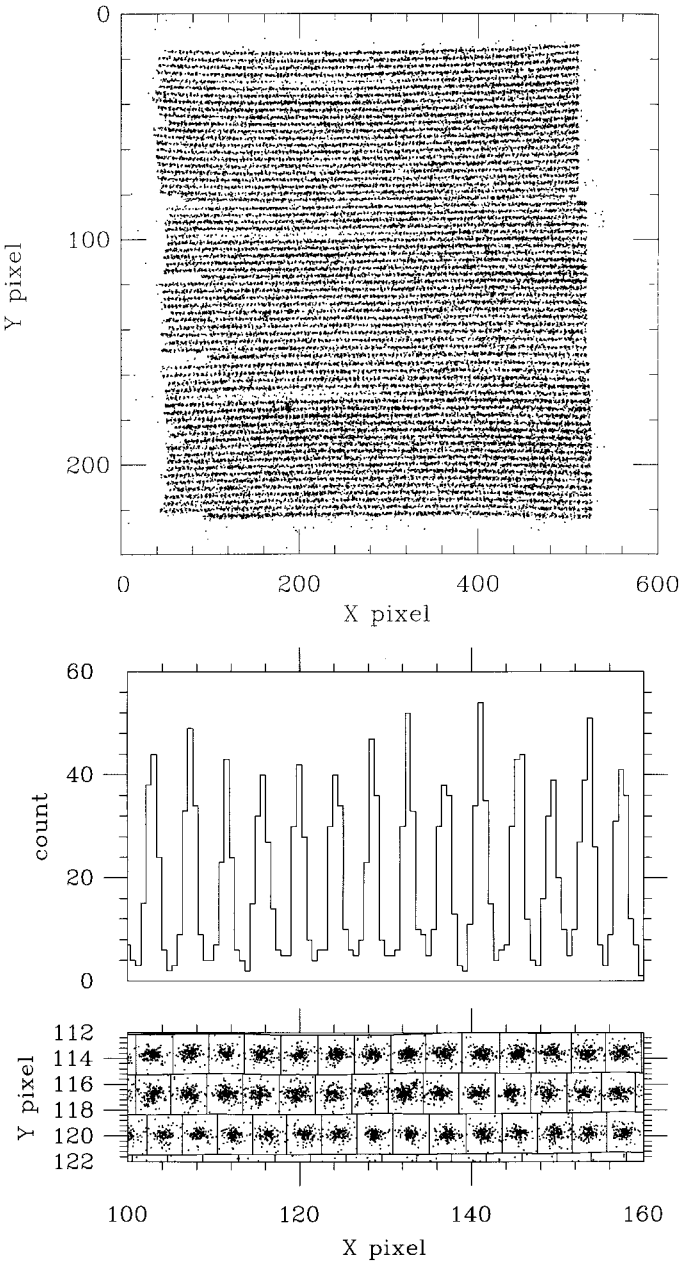

Figure 24. SOFT calibration using a heavy ion beam from the MSU/NSCL accelerator. The top panel is a cross plot of pixel cluster centroids in CCD pixel space. This figure is a superposition of many events obtained by scanning an oxygen beam over the full 26 cm × 26 cm area of the fiber hodoscope. Each row of dots in this view corresponds to a single fiber tab of width ∼2.4 cm. The bottom panel shows an expanded view of a small region in pixel space. It is seen from the cross plots that the individual fibers are clearly resolved. The histogram in the middle panel is obtained by summing the number of counts in each column for the y-pixel range from about 112 to 115. Fits to the peaks (in both the x and y dimensions) are used to derive a map of the relationship between fiber number and pixel location and establish the boundaries between fibers in the CCD image, as indicated by the grid in the bottom panel.

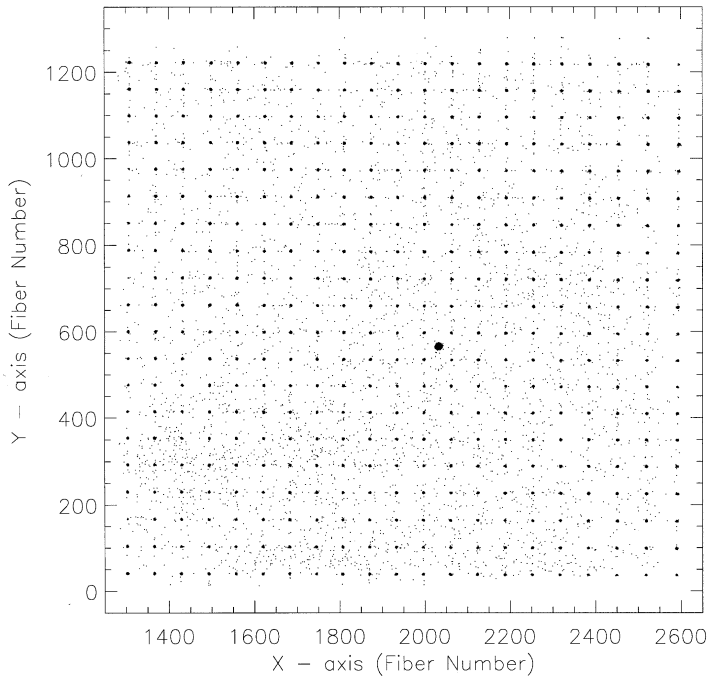

Figure 25. Absolute position calibration of SOFT. A lead mask with 1 mm diameter holes drilled on a 1.27 cm × 1.27 cm grid was used to obtain the fiber to real-space map. The regularly spaced dark spots are the superposition of events which passed through the holes. The vast majority of the events fall in these spots, which are heavily saturated in this image. The sprinkling of particles between the holes is due, in part, to nuclei which interacted in the lead plate producing long-range fragments which penetrate the plate. The large spot slightly offset from the center is the image of a 3 mm hole included for the purpose of determining the mask orientation.

In the course of calibrating the SOFT system it was observed that occasionally an otherwise-good cluster would be displaced significantly from the correct track. This has been traced to an electron 'hopping' phenomenon in which a photoelectron strikes the solid matrix of the microchannel plate and bounces into a channel up to several hundred microns away. While unimportant for heavy nuclei where the cluster centroid is derived from a large number of photoelectrons, electron hopping can affect the tracking of the lightest elements. The SOFT hodoscope was intentionally designed with the H2 plane not equidistant from the H1 and H3 planes (see Figure 6) to aid in determining which of the three layers was affected in events where hopping has altered one of the coordinate measurements. Preliminary techniques for identifying and recovering events in which hopping has occurred have been implemented.

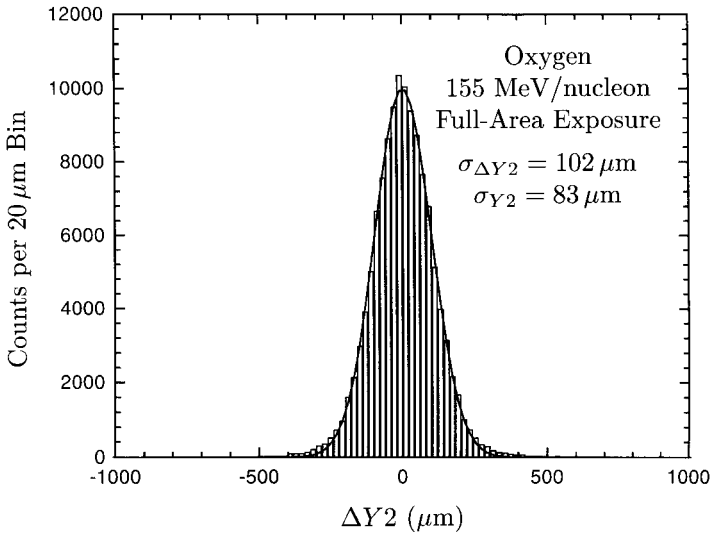

Figure 26. SOFT position resolution obtained using oxygen nuclei at ~155 MeV nucl^{-1}. These events were collected over the full active area of the fiber plane. The distribution is obtained using the method of residuals (see text) and shows that a resolution ~83 μm was obtained in one coordinate.

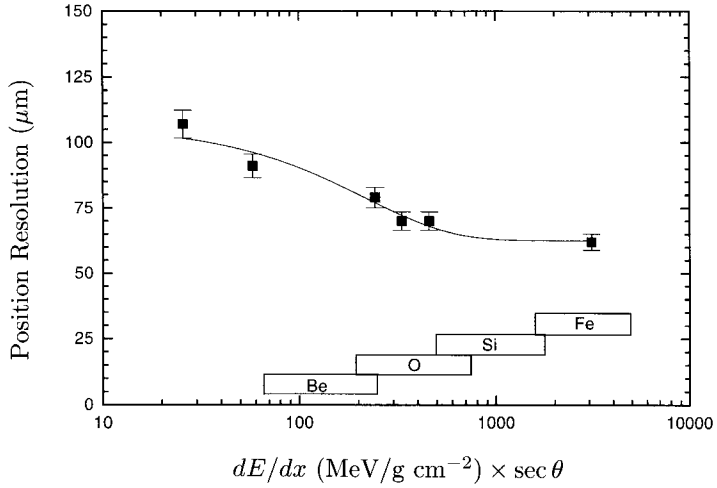

Figure 27. SOFT position resolution as a function of dE/dx·sec θ, which is proportional to the energy loss in the fiber plane. The position resolution was obtained using beams of He, Li, C, N, O, and Ar nuclei (data points from left to right) with energy at the top of the instrument of 155 MeV nucl^{-1}. The particles were collected over an area ~ 2 cm corresponding to the diameter of the beam spot. The bars along the abscissa indicate the range covered for several elements in flight.

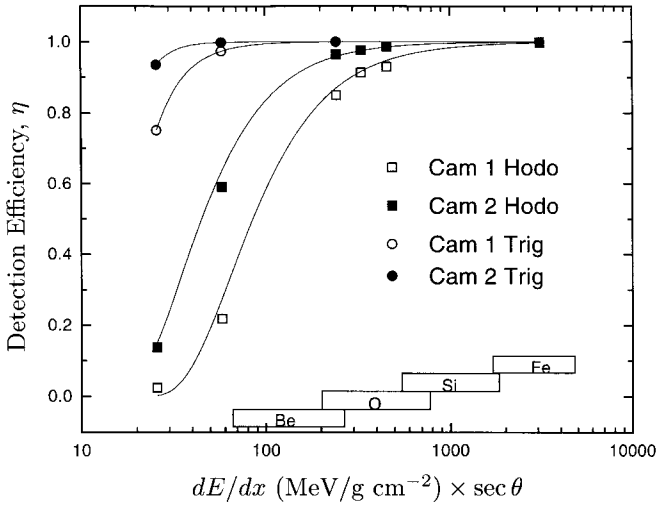

Figure 28. SOFT detection efficiencies as a function of the energy loss in SOFT. The hodoscope and trigger detection efficiencies were obtained from an MSU/NSCL exposure using 155 MeV nucl^{-1} He, Li, C, N, O, and Ar nuclei (data points from left to right) incident at angles $\theta_x = \theta_y = 15°$. The hodoscope efficiencies are for '6-layer events' (i.e., events with fiber hits that lie along a straight-line trajectory in each of the six hodoscope layers). The trigger fiber efficiencies which are plotted are based on the logical OR of the Tx and Ty fiber layers. The bars along the abscissa indicate the range covered for several elements in flight.

9.4. DETECTION EFFICIENCY

The detection efficiencies of the hodoscope and trigger fibers were also measured for a range of nuclei. Coordinates were derived for the brightest cluster in each of the 6 layers, and the next 6 brightest clusters independent of layer. Events having good straight-line fits to centroids in each of the 6 layers were considered detected, and the ratio of this number to the total number of events in the data set was defined as the 6-layer detection efficiency (η). Figure 28 shows the resulting efficiencies as a function of the energy loss in SOFT.

Camera B, which has higher efficiency than Camera A, is used as the default camera, although either camera has adequate efficiency for measuring beryllium and heavier elements. The difference in efficiencies is thought to be due to differences between the fiber-optic face-plates used on the image intensifiers (Hink et al., 1996). Efficiencies for '5-layer events' are significantly greater but the event quality has not yet been studied in detail.

Figure 28 also shows the trigger-detection efficiency, which is defined as the fraction of events in which a particle was detected in at least one of the two trigger planes, since in flight the SOFT trigger is normally formed from the logical OR of the Tx and Ty signals. Trigger efficiencies using either SOFT camera are near 100% for Be and heavier nuclei.

10. Conclusions

The Cosmic-Ray Isotope Spectrometer was launched aboard the Advanced Composition Explorer spacecraft on 25 August 1997 and was turned on two days later. At the time of submission of this manuscript nearly two months of CRIS data had been returned from space. Preliminary analysis of these data indicates that CRIS has achieved essentially all of the design goals discussed above. It is expected that continued data collection over a period of several years will result in a data set with excellent mass resolution and unprecedented statistical accuracy that can be used to make major advances in understanding the astrophysics of galactic cosmic rays.

Acknowledgments

This research was supported by the National Aeronautics and Space Administration at the Space Radiation Laboratory (SRL) of the California Institute of Technology (under contract NAS5–32626 and grant NAGW-1919), the Jet Propulsion Laboratory (JPL), the Goddard Space Flight Center (GSFC), and Washington University.

We wish to thank the many individuals and organizations who made important contributions to the development of CRIS: J. H. Marshall III of Radcal Corp., J. Gill and B. Mitchell of Harris Corp., and R. McKenzie of Teledyne Corp. played major roles in the design, development, and fabrication of the custom VLSI chips and hybrid circuits, while G. Stupian and M. Leung of Aerospace Corp. provided their micro-focus x-ray facility for hybrid screening. J. Walton and his group at Lawrence Berkeley National Laboratory fabricated the silicon detectors. D. Aalami of Space Instruments was responsible for the design of the power supplies and also contributed to the design, fabrication, and testing of the other electronic assemblies. W. Blanchard of Falcon Services provided all of the board layouts except for the logic board, which was provided by J. Stelma of Design Solutions. Electronic assembly was carried out at Caltech and JPL by N. Neverida and T. Ngo-Luu of JPL with the help of T. Dea, who also assisted during conformal coating and environmental testing at JPL. V. Nguyen of Caltech was responsible for most of the subassembly testing. W. Morris of Caltech received and kitted parts and J. Valenzuela of Space Instruments assisted in PCB production and technical document control. B. Williams of JHU/APL was responsible for the thermal design and support.

At Caltech, B. Sears, R. Selesnick, J. Cummings, and L. Sollitt provided calibration and analysis support, G. Allbritton was responsible for detector testing, G. Flemming contributed to the flight software, J. Burnham provided engineering support, F. Spalding was responsible for project administration, and D. Kubly and R. Kubly performed a variety of secretarial tasks. In addition, M. Calderon, A. Davis, and T. Garrard assisted with computing issues, R. Paniagua and R. Borup

provided support in the Caltech Physics shop, and B. Wong helped with a variety of laboratory tasks. J. Lopez-Tiana and E. Friese provided purchasing and contract support.

At JPL, B. Potter assisted in expediting the VLSI build at Harris Corp., D. Cipes-Cwik and R. Hill carried out the hybrid inspections at Teledyne, N. Silva contributed to the assembly of the telescope modules and instrument card cage, as well as development of specifications for magnetics parts, W. Powell served as instrument expeditor, K. Evans provided advice on parts, J. DePew provided technical support for calibrations and laboratory testing, and M. Salama and T. Scharton assisted with mechanical design issues along with P. Rentz of EER Systems Corporation. R. Pool consulted on contractual issues.

At Washington University, G. Simberger was responsible for parts procurement, electronics construction, and inspection. D. Braun was responsible for the organization and inspection of the mechanical parts, the fabrication of the fibers, and the assembly of the fiber planes. J. Cravens of Southwest Research performed the quality assurance on SOFT and provided inputs on the use of image intensifiers in space. H. Darlington of JHU/APL contributed to the design and development of the image intensified CCD cameras. S. Battel of Battel Engineering contributed to the high voltage power supply development. T. Soulanille of Altadena Instruments performed a design review for the camera electronics system. L. Geer, presently at the National Institute of Health, had the original idea to use a photodiode coupled to the image intensifiers for triggering. T. Hardt, D. Steelman, D. Huelsman, and A. Biondo fabricated substantial portions of the SOFT detector in the Washington University machine shop. D. Yates, J. Jarrell, and C. Kruger provided support with contracting, accounting, and proposal preparation. J. Howorth, D. Wilcox, and their staff at Photek developed the image intensifiers and provided helpful advice on the technical details of image intensifiers. G. M'Sadoques of K&M Electronics designed the image intensifier high-voltage power supplies, which were also fabricated by the same company.

At GSFC, B. Fridovich provided administrative support, M. Madden and B. Nahory were responsible for detector testing, and S. Hendricks of Swales and Associates, Inc. assisted with mechanical design issues.

Accelerator testing of the CRIS detectors was made possible by N. Anantaraman, R. Ronningen, and the staff of the National Superconducting Cyclotron Laboratory at Michigan State University, while H. Specht, D. Schardt, and the staff of the GSI heavy ion accelerator in Darmstadt, Germany made possible the heavy ion calibrations of the completed CRIS instrument.

The spacecraft team at JHU/APL provided assistance in many areas while CRIS was being integrated and tested on the spacecraft.

Finally, we thank A. Frandsen, G. Murphy, H. Eyerly, M. Breslof, C. Rangel, and M. McElveney of the ACE Payload Management Office for their untiring support and assistance, and D. Margolies, J. Laudadio, and the ACE Project Office at GSFC for their help in all phases of the CRIS development.

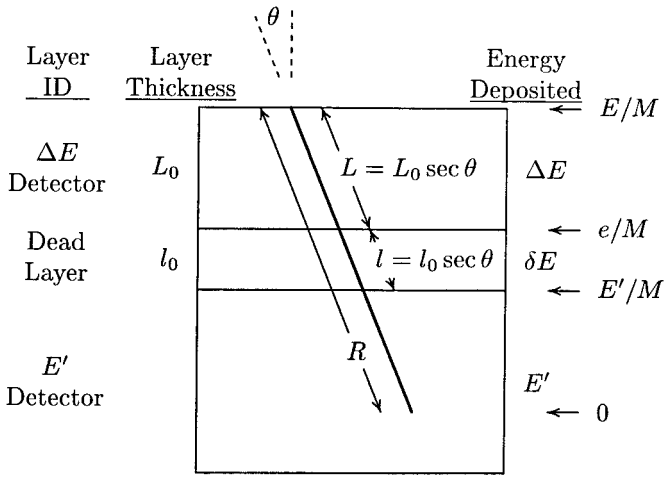

Figure 29. Schematic illustration of 2-detector energy loss vs. residual energy measurement defines the quantities used in calculating mass resolution. The heavy line represents the track of a particle in the detector layers. The far-right column shows the variables used to represent the particle's energy per nucleon at each of the detector interfaces. The layer dimensions are not drawn to scale.

Appendix A. Mass Resolution Calculations

As discussed in Section 3.1, the derivation of a particle's mass using the ΔE vs residual energy technique is based on the fact that the change in the particle's range in penetrating a detector is equal to the thickness of material penetrated. The quantities of interest are defined in Figure 29. Here we consider only the case of two energy measurements, ΔE and E'. In an instrument like CRIS where one has energy loss measurements in a larger number of layers, successive layers can be combined to obtain an equivalent two-detector configuration for which we can analyze the mass resolution using the formulas presented below.

Using $\mathcal{S}_Z(\epsilon)$ to denote the functional dependence of the specific ionization $(\mathrm{d}E/\mathrm{d}x)$ of a nucleus of atomic number Z on the particle's energy per nucleon ϵ, the range of a nucleus with charge and mass numbers Z and M_0 is $\mathcal{R}_{Z,M_0}(\epsilon) = M_0 \int_0^{\epsilon} d\epsilon'/\mathcal{S}(\epsilon')$. The range for another isotope (mass M) of the same element can be obtained by scaling: $\mathcal{R}_{Z,M}(\epsilon) = (M/M_0)\,\mathcal{R}_{Z,M_0}(\epsilon)$. Finally, the function $\mathcal{E}_{Z,M_0}(R)$ is defined to be the inverse of $\mathcal{R}_{Z,M_0}(\epsilon)$. These three related functions, $\mathcal{S}$, $\mathcal{R}$, and $\mathcal{E}$, are available in tabular or semi-empirical form.

Taking into account the dead layer of thickness l, one has two equations relating range differences to thickness penetrated:

$$\mathcal{R}_{Z,M_0}\left(\frac{\Delta E + \delta E + E'}{M}\right) - \mathcal{R}_{Z,M_0}\left(\frac{E'}{M}\right) = \frac{M_0}{M}\,(L + l)\,, \tag{4}$$

$$\mathcal{R}_{Z,M_0}\left(\frac{\delta E + E'}{M}\right) - \mathcal{R}_{Z,M_0}\left(\frac{E'}{M}\right) = \frac{M_0}{M}\,l\,. \tag{5}$$

TABLE VIII
Partial derivatives used in mass resolution calculations

Derivative	General expression[a]
$\frac{\partial M}{\partial \Delta E}$	$M\frac{1}{\mathbf{X}\mathcal{S}_Z(E/M)}$
$\frac{\partial M}{\partial E'}$	$M\left(\frac{\mathcal{S}_Z(e/M)}{\mathcal{S}_Z(E/M)}-1\right)\frac{1}{\mathbf{X}\mathcal{S}_Z(E'/M)}$
$\frac{\partial M}{\partial L}$	$-M\frac{1}{\mathbf{X}}$
$\frac{\partial M}{\partial l}$	$M\left(\frac{\mathcal{S}_Z(e/M)}{\mathcal{S}_Z(E/M)}-1\right)\frac{1}{\mathbf{X}}$

[a]Expressions involve a common factor with dimensions of thickness:
$\mathbf{X}\equiv\left[\frac{\Delta E}{\mathcal{S}_z(E/M)}+\left(\frac{\mathcal{S}_Z(e/M)}{\mathcal{S}_Z(E/M)}-1\right)\frac{E'}{\mathcal{S}_Z(E'/M)}-L+\left(\frac{\mathcal{S}_Z(e/M)}{\mathcal{S}_Z(E/M)}-1\right)l\right]$.

Eliminating the unknown energy loss (δE) in the dead layer between these two equations yields the basic relation needed for calculating mass resolution:

$$\frac{\Delta E}{M} = \mathcal{E}_{Z,M_0}\left(\mathcal{R}_{Z,M_0}\left(\frac{E'}{M}\right)+\frac{M_0}{M}(L+l)\right) - \mathcal{E}_{Z,M_0}\left(\mathcal{R}_{Z,M_0}\left(\frac{E'}{M}\right)+\frac{M_0}{M}l\right). \quad (6)$$

This equation gives M implicitly in terms of the measured quantities ΔE, E', L, and l. Table VIII lists the various partial derivatives needed for calculating the effect on mass resolution due to errors in these quantities.

The following sections discuss the calculation of the contributions to the overall mass resolution caused by various sources of error.

A1. Bohr/Landau fluctuations

The energy loss of a heavy nucleus in matter is the result of large numbers of Coulomb collisions with electrons in the material. As such it is a statistical process subject to fluctuations. For the energies and atomic numbers of interest for CRIS the distribution of energy losses in a thin layer of thickness x is Gaussian with r.m.s. width $\sqrt{(\mathrm{d}\sigma^2_{\Delta E}/\mathrm{d}x)_{\mathrm{Landau}}\,x}$, where

$$\left(\frac{\mathrm{d}\sigma^2_{\Delta E}}{\mathrm{d}x}\right)_{\mathrm{Landau}} = Z^2\,\frac{(0.396\ \mathrm{MeV})^2}{\mathrm{g\ cm^{-2}}}\,\frac{Z_{\mathrm{m}}}{A_{\mathrm{m}}}\,\frac{\gamma^2+1}{2} \quad (7)$$

is the increase in the variance of the energy loss per unit path length traversed (Rossi, 1952). In this equation, γ is the Lorentz factor corresponding to the particle's energy per nucleon, Z is the particle's charge, and Z_{m} and A_{m} are the charge

and mass numbers of the medium. For a particle penetrating a ΔE detector which is not thin compared to the particle's range, one must take into account the effects both of the variation of the particle's energy as it slows and of correlations between energy losses at different depths in the detector (Payne, 1969). In this case one obtains the result:

$$\sigma_{\Delta E(\text{Landau})} = \sqrt{M \int_{e/M}^{E/M} \frac{\mathcal{S}_Z^2(e/M)}{\mathcal{S}_Z^3(\epsilon)} \left(\frac{\mathrm{d}\sigma_{\Delta E}^2}{\mathrm{d}x}\right)_{\text{Landau}} \mathrm{d}\epsilon}. \tag{8}$$

A.1.1. *Bohr/Landau Fluctuations in the ΔE Detector*

The fluctuation of a particle's energy loss in the ΔE detector results in an equal and opposite fluctuation in the residual energy E'^*. Thus the contribution of Landau fluctuations in the ΔE detector to the mass resolution is given by

$$\sigma_{M,\text{Landau in } L} = \left(\frac{\partial M}{\partial \Delta E} - \frac{\partial M}{\partial E'}\right) \sigma_{\Delta E(\text{Landau})}. \tag{9}$$

A.1.2. *Bohr/Landau Fluctuations in the Dead Layer*

The fluctuation of the energy loss in the dead layer appears only as a fluctuation in the residual energy (since the loss in the dead layer itself is not measured). This fluctuation, $\sigma_{\delta E(\text{Landau})}$, is given by an expression analogous to Equation (9) but with limits of integration E'/M and e/M. The resulting contribution to the mass resolution is

$$\sigma_{M,\text{Landau in } l} = -\frac{\partial M}{\partial E'} \sigma_{\delta E(\text{Landau})}. \tag{10}$$

A.2. Multiple Coulomb scattering

Coulomb collisions of the energetic nucleus with nuclei and electrons in the ΔE detector cause small deflections in the particle's trajectory. The 'multiple scattering' resulting from the cumulative effects of many such interactions alters the path length in the detector. When an energetic nucleus traverses a small thickness, x, of material the distribution of emerging trajectories has a projection on a plane containing the incoming trajectory which is approximately Gaussian, centered on the direction of the incoming trajectory, and having an r.m.s. angular width given by $\sqrt{\left(\mathrm{d}\sigma_{\delta\theta}^2/\mathrm{d}x\right)\, x}$, where

$$\frac{\mathrm{d}\sigma_{\delta\theta}^2}{\mathrm{d}x} \simeq \left(\frac{Z}{M} \frac{0.0146}{\beta^2\gamma}\right)^2 \frac{1}{X_0} \tag{11}$$

* We assume that the dead layer thickness is small and the energy loss in the dead layer is not significantly affected by the fluctuation of the energy loss in the ΔE detector.

is the increase in the variance of the angular distribution (measured in radians), projected on a plane containing the incident trajectory, per unit path length traversed (Barnett et al., 1996). Here Z and M are the charge and mass numbers of the energetic nucleus, γ is its Lorentz factor, β is the corresponding velocity divided by the speed of light, and X_0 is the radiation length in the medium. For silicon, $X_0 = 21.82$ g cm^{-2}.

In the case where the thickness of the ΔE detector is sufficiently thin that the change of $\beta^2\gamma$ in it can be neglected, this angular deflection results in an r.m.s. path length error, σ_L, given by $\sigma_{L\ (\mathrm{scat})} = (1/\sqrt{3})\, L\, \tan\theta \sqrt{\left(\mathrm{d}\sigma^2_{\delta\theta}/\mathrm{d}x\right) x}$. When the change of the $\beta^2\gamma$ factor as the particle slows in the ΔE detector cannot be neglected, this result is replaced by an integral

$$\sigma_{L\ (\mathrm{scat})} = L \tan\theta \sqrt{M} \times \times \sqrt{\int_{E'/M}^{E/M} \left(\frac{\mathcal{R}(E/M) - \mathcal{R}(\epsilon)}{L}\right)^2 \left(\frac{\mathrm{d}\sigma^2_{\delta\theta}}{\mathrm{d}x}\right)_{\epsilon} \frac{\mathrm{d}\epsilon}{\mathcal{S}_Z(\epsilon)}}\,. \tag{12}$$

The change in the particle's path length in the ΔE detector due to multiple scattering leads to a mass error given by

$$\sigma_{M,\ \mathrm{scat}} = \frac{\partial M}{\partial L}\, \sigma_{L\ (\mathrm{scat})}. \tag{13}$$

A.3 Trajectory measurement errors

Measured trajectories are used in two ways in the mass calculation. The slope of the particle's track is used in calculating the $\sec\theta$ factor needed to obtain a particle's path length in the ΔE detector. The extrapolation of the trajectory to the point at which it intercepts a given detector is used to look up from the calibration maps the detector thickness and dead layer at the point of penetration. Thus uncertainties in both the slope and the intercept of the trajectory contribute to the mass resolution.

To assess these contributions, it is assumed that the trajectory is derived from measurements of two or more pairs of orthogonal coordinates, x_i and y_i ($i = 1 \ldots n$), made at heights z_i above the energy loss detectors. The measurements at height z_i are made with r.m.s. errors σ_{x_i} and σ_{y_i}. The projection of the trajectory on the xz plane is obtained from a fit of x_i vs z_i weighted proportional to $1/\sigma^2_{x_i}$, and similarly for the yz projection. The slope, $\mathrm{d}x/\mathrm{d}z$, of the fitted line has uncertainty

$$\sigma_{\mathrm{d}x/\mathrm{d}z} = \left[\sum_{i=1}^{n} \frac{1}{\sigma^2_{x_i}}\, (z_i - \mathbf{Z}_x)^2\right]^{-1/2}, \tag{14}$$

with the definition $\mathbf{Z}_x \equiv \sum_{i=1}^{n}(z_i/\sigma^2_{x_i}) / \sum_{i=1}^{n}(1/\sigma^2_{x_i})$.

Furthermore the uncertainty in $x_0(z)$, the x intercept of the fitted trajectory at depth z, is given by

$$\sigma_{x_0(z)} = \sigma_{\overline{x}} \sqrt{\frac{\sum_{i=1}^{n}(z_i - z)^2/\sigma_{x_i}^2}{\sum_{i=1}^{n}(z_i - \mathbf{Z}_x)^2/\sigma_{x_i}^2}}, \tag{15}$$

with the definition $\sigma_{\overline{x}} \equiv \left(\sum_{i=1}^{n} 1/\sigma_{x_i}^2\right)^{-1/2}$.

In the case of CRIS these expressions can be simplified by assuming that all coordinate measurement uncertainties are equal (we will denote them by σ_x) and that coordinate pairs (x_i, y_i) are measured at the same height z_i in the instrument. One then finds $\mathbf{Z}_x = \mathbf{Z}_y \equiv \mathbf{Z} = (\sum_{i=1}^{n} z_i)/n$, $\sigma_{\overline{x}} = \sigma_x/\sqrt{n}$,

$$\sigma_{\mathrm{d}x/\mathrm{d}z} = \sigma_{\mathrm{d}y/\mathrm{d}z} = \frac{\sigma_x}{\sqrt{\sum_{i=1}^{n}(z_i - \mathbf{Z})^2}}, \tag{16}$$

and

$$\sigma_{x_0(z)} = \sigma_{y_0(z)} = \frac{\sigma_x}{\sqrt{n}} \sqrt{\frac{\sum_{i=1}^{n}(z_i - z)^2}{\sum_{i=1}^{n}(z_i - \mathbf{Z})^2}}. \tag{17}$$

The $\sec\theta$ factor used in calculating a particle's path length in the ΔE detector can be written in the form $\sec\theta = [1 + (\mathrm{d}x/\mathrm{d}z)^2 + (\mathrm{d}y/\mathrm{d}z)^2]^{1/2}$, and under the assumptions used for deriving Equation (17), has fractional uncertainty given by

$$\frac{\sigma_{\sec\theta}}{\sec\theta} = \frac{1}{2} \sin 2\theta \, \sigma_{\mathrm{d}x/\mathrm{d}z}. \tag{18}$$

Further simplification is realized if there are only two trajectory measurement planes or if there are three planes with one placed midway between the other two (nearly the case in CRIS). In this case $\sigma_{\mathrm{d}x/\mathrm{d}z} = \sqrt{2}\,\sigma_x/\Delta z$, where Δz is the spacing between the outermost two trajectory planes, and one obtains

$$\frac{\sigma_{\sec\theta}}{\sec\theta} = \frac{1}{\sqrt{2}} \sin 2\theta \, \frac{\sigma_x}{\Delta z}. \tag{19}$$

The error in $\sec\theta$ makes (correlated) contributions to the mass resolution due to its effects on the path lengths in both the ΔE detector and in the dead layer:

$$\sigma_{M,\sec\theta} = \frac{\partial M}{\partial L} L_0 \, \sigma_{\sec\theta} + \frac{\partial M}{\partial l} l_0 \, \sigma_{\sec\theta}. \tag{20}$$

The uncertainties in the intercepts of the derived trajectory contribute to the mass resolution through their effects on the accuracy with which thickness can be obtained from the detector calibration maps. This is discussed in the following section.

A.4 MAPPING ERRORS

Maps of the detector thickness, $L_j(x, y)$, and dead layer, $l_j(x, y)$, (with j labeling the detector number) are obtained from laboratory and accelerator measurements. They are used, in conjunction with the measured particle trajectory, to derive the path lengths for calculating particle charge and mass. Thickness errors arise due both to uncertainties in the measured maps and to uncertainties in the location at which the trajectory penetrated the detector. The overall thickness mapping error can be expressed as the sum of three uncorrelated contributions, $\sigma^2_{L(\text{map})} = \sigma^2_{L(\text{map}),L_0} + \sigma^2_{L(\text{map}),x} + \sigma^2_{L(\text{map}),y}$. When the ΔE measurement is obtained by summing signals from m successive detectors located in the stack at positions $z_1, \ldots, z_m$, these contributions can be calculated as:

$$\sigma^2_{L(\text{map}),L_0} = \sum_{j=1}^{m} \sigma^2_{L_j}, \tag{21}$$

$$\sigma^2_{L(\text{map}),x} = \left(\sum_{j=1}^{m} \frac{\partial L_j}{\partial x} \sigma_{x_0(z_j)} \right)^2, \tag{22}$$

$$\sigma^2_{L(\text{map}),y} = \left(\sum_{j=1}^{m} \frac{\partial L_j}{\partial y} \sigma_{y_0(z_j)} \right)^2. \tag{23}$$

In these expressions, each partial derivative is evaluated at the location where the particle penetrated that particular detector.

The errors related to the application of the dead-layer map are obtained from similar expressions with l substituted for L and with the locations z_j appropriate to the position of the dead layer in the stack. As noted above, only the dead layer between the ΔE and E' measurements is taken into account in this analysis; thus the sum over the individual detectors that contribute to the ΔE measurement is not required. The contributions caused by trajectory errors introduce correlations between the thickness and dead layer uncertainties.

Mapping errors (both for thickness and dead layer) make an overall contribution to mass resolution given by:

$$\sigma^2_{M(\text{map})} = \left(\frac{\partial M}{\partial L} \right)^2 \sigma^2_{L(\text{map}),L_0} + \left(\frac{\partial M}{\partial l} \right)^2 \sigma^2_{l(\text{map}),l_0} +$$

$$+\left(\frac{\partial M}{\partial L}\sigma_{L(\text{map}),x}-\frac{\partial M}{\partial l}\sigma_{l(\text{map}),x}\right)^2+$$

$$+\left(\frac{\partial M}{\partial L}\sigma_{L(\text{map}),y}-\frac{\partial M}{\partial l}\sigma_{l(\text{map}),y}\right)^2. \tag{24}$$

When designing an instrument, one normally cannot predict the directions of the thickness gradients or their correlations between different layers. Thus, in practice, the possible correlations between different contributions to the mapping error are neglected and all contributions are compounded as if uncorrelated. In addition, although correlations between the mapping errors and sec θ errors are present since they depend on the same trajectory measurements, these correlations are neglected because their relative signs are not known.

A.5 Energy measurement errors

The measurement of the energy deposited in a detector or in a combination of detectors associated with a single pulse-height analyzer (PHA) is uncertain due both to the contribution of electronic noise and to the finite channel width used in digitizing the signal. For the kth PHA the energy error can be written

$$\sigma_{E_k}^2=\sigma_{E_k(\text{noise})}^2+\left(\frac{w_k}{\sqrt{12}}\right)^2, \tag{25}$$

where w_k is the channel width for this PHA. The uncertainties associated with the measurements of ΔE and E' are sums in quadrature of the values of $\sigma_{E_k}^2$ from all the PHAs whose outputs are summed to form these quantities. The corresponding contributions to the mass resolution are:

$$\sigma_{M(\Delta E\text{ meas.})}=\frac{\partial M}{\partial \Delta E}\sqrt{\sum_{k\in\Delta E}\sigma_{E_k}^2}, \qquad \sigma_{M(E'\text{ meas.})}=\frac{\partial M}{\partial E'}\sqrt{\sum_{k\in E'}\sigma_{E_k}^2}. \tag{26}$$

A.6 Additional effects

Several potential sources of mass uncertainty are omitted in our resolution calculations because they should be correctable using calibrations that can be obtained from laboratory or flight data. Effects of this type include: small rotations or displacements of the silicon detectors from their nominal placement in the stack, effects of non-linearities in the transfer functions of the pulse-height analyzers, and imperfections in the geometry of the hodoscope.

The effects of multiple Coulomb scattering in the hodoscope have also been neglected. These should be rather insignificant for the CRIS instrument due to the small amount of material above the Si(Li) detector stack.

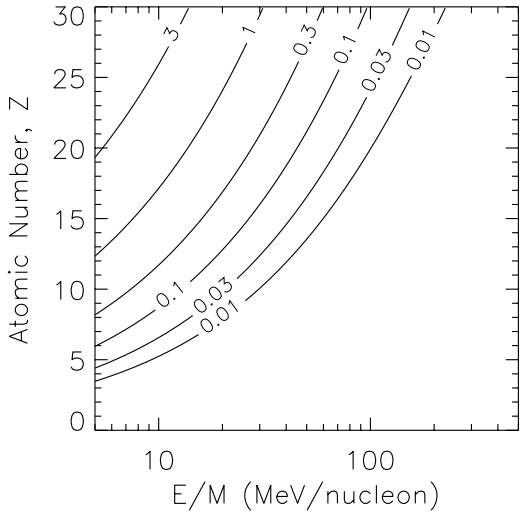

Figure 30. Contour plot of the difference between a particle's atomic number, Z, and its effective charge, $q_{\rm eff}$, as a function of atomic number and particle energy per nucleon. This difference is caused by the attachment of atomic electrons. In regions of the plot where $Z - q_{\rm eff} \gtrsim 1$ one expects that charge-state fluctuations could contribute significantly to the width of the energy loss distribution, and therefore to the mass resolution.

For heavy elements at low energy, the nuclei will have several electrons attached (Ahlen, 1980). For example, the effective charge of an iron ($Z = 26$) nucleus at 20 MeV nucl^{-1} is only $+24.9$. The average effect of the reduced charge on the particle's slowing is taken into account in the range energy relation that is used. However, the charge state is subject to statistical fluctuations as collisions cause attachment and stripping of electrons. These fluctuations, which should be added in quadrature to the Bohr/Landau fluctuations discussed above, have been neglected due to lack of data on the magnitude of the effects. Preliminary measurements in the regime where charge-state fluctuations should be significant suggest that calculations neglecting this effect fail to adequately account for the observed mass resolution. Figure 30 shows the amount by which the effective charge, $q_{\rm eff}$, is expected to differ from fully stripped for various combinations of Z and E/M. When this difference $Z - q_{\rm eff} \ll 1$, the calculations presented above should adequately account for the overall mass resolution. This condition is generally met for the particles of interest in CRIS, but can be more important for the lower-energy nuclei being studied with the Solar Isotope Spectrometer (see Stone et al., 1998, this issue).

A.7 Monte Carlo calculations

The above analytic treatment of the mass resolution is particularly useful for assessing the functional dependence of the resolution on the various parameters involved in the instrument design. As an alternative, one can carry out Monte Carlo sim-

ulations of the instrument response. The Monte Carlo approach allows one to readily average over particle parameters such as energy and incidence angle that will be encountered in flight. Both approaches were employed in designing the CRIS instrument, with generally consistent results.

Appendix B. CRIS Logic Equations

The triggering of the CRIS instrument and the determination of whether a valid event has occurred are based on boolean logic implemented using Actel gate arrays. The inputs to the logic circuits consist of discriminator pulses (some latched) from the instrument sensors, signals from the on-board stimulus and hazard circuits, and various static control bits that can be set by command. Table IX defines these inputs and Table X lists the logic equations that use these signals to determine when trigger and valid coincidence conditions are met.

The logic is designed to distinguish, approximately, among hydrogen ($Z = 1$), helium ($Z = 2$) and heavier nuclei ($Z > 2$) based on appropriately set medium level ('m') and high level ('h') discriminators. Whereas the normal coincidence requires that heavy nuclei trigger at least the E1 and E2 discriminators, an additional term ('adc2') is used to accept candidate hydrogen and helium nuclei based on triggering any two successive discriminators. This term makes it possible to include light nuclei which stop deep in the stack and do not trigger the front detectors. Pulse heights from all the detectors are, nevertheless measured (whether or not the discriminator was triggered) and are available for analysis of the event.

Appendix C. CRIS Normal Event Format

Table XI summarizes the format used for transmission of CRIS normal events. Each event starts with a fixed–length, 6–byte header, the first byte of which gives the total length of that event. As shown in Table XI, the header also indicates whether or not various optional subfields of data are included in that event, and the sizes of the variable length subfields. Among other things, the header specifies whether pulse height data from both the A/B and C/D telescopes are included, how many guard detectors were triggered and whether or not the guard pulse heights are being transmitted, the 'range' of the particle (that is, the identity of the deepest triggered detector), the number of position coordinates returned from SOFT, and the time (in instrument cycles) that the event was put into the event buffer (which is needed to match the event with the appropriate rate sample and live time). If data from both telescope pairs are included in the event, this primary header is followed by a one-byte secondary header, which lists the number of guards triggered and the range of the particle in the second telescope pair.

TABLE IX
CRIS logic inputs[a]

Signal	Description
Active inputs	
e1a, e1b, e2ab, . . ., e9ab	low level discriminator signals from Si(Li) detector center PHAs
e1ma, e1mb, e2mab, . . ., e8mab	medium level discriminator signals from Si(Li) detector center PHAs
e1ha, e1hb, e2hab, . . ., e8hab	high level discriminator signals from Si(Li) detector center PHAs
g2ab, g3ab, . . ., g7ab	low level discriminator signals from Si(Li) detector guard PHAs
g2hab, g3hab, . . ., g7hab	high level discriminator signals from Si(Li) detector guard PHAs
Static inputs (commandable) [b]	
e1_mode	set to require that only e1a or e1b be present; cleared to allow both to be present (and similarly for e1c and e1d)
force_e1a	set to override requirement that e1a be present (similarly for *force_e1b*, *force_e2ab*)
delete_g2ab	set to override requirement that g2ab not be present (similarly for *delete_g3ab* through *delete_g7ab*)
unforce_e3ab	set to require that e3ab be present for a valid event in AB telescope pair (similarly for *unforce_e3ab* through *unforce_e8ab*)
adc2ab_disable	set to disallow as valid any events with low-level discriminator triggers from any two successive detectors
hmode0, hmode1	select one of four possible modes for trigger from SOFT hodoscope: x plane independent of y plane, y independent of x, either x or y, both x and y
force_hodo	set to override requirement that SOFT trigger be present for coincidence
hy_enable	set to allow events tentatively identified as hydrogen ($Z = 1$)
he_enable	set to allow events tentatively identified as helium ($Z = 2$)
stim_always_valid	set to treat all pulser stimulus events as valid; cleared to require that they satisfy the same coincidence requirements as particle events
haz_anti_en	set to allow hazard signal to veto events

[a]Inputs are listed only for the AB telescope pair. Corresponding signals exist from the CD telescope pair.
[b]Other command bits exist which allow any active input to be disabled and provide additional control of the logic, as described in note c to Table X.

TABLE X
CRIS logic equations

Term[a]	Definition[b]	Comments
[e1a]	(e1a · $\overline{\text{e1b}}$ · *e1_mode* + e1a · $\overline{\textit{e1\_mode}}$) + *force_e1a*	
[e1b]	(e1b · $\overline{\text{e1a}}$ · *e1_mode* + e1b · $\overline{\textit{e1\_mode}}$) + *force_e1b*	
glab	g2ab · $\overline{\textit{delete\_g2ab}}$ + g3ab · $\overline{\textit{delete\_g3ab}}$ + · · · + g7ab · $\overline{\textit{delete\_g7ab}}$	any low-level ab guard discr.
[e2ab]	e2ab + $\overline{\textit{force\_e2ab}}$	
/e3ab/	e3ab + $\overline{\textit{unforce\_e3ab}}$	similar for e4ab . . . e8ab
minrngab	([e1a] + [e1b]) · [e2ab] · /e3ab/ · /e4ab/ · /e5ab/ · /e6ab/ · /e7ab/ · /e8ab/	
adc2ab	((e1a + e1b) · e2ab + e2ab · e3ab + e3ab · e4ab + e4ab · e5ab + e5ab · e6ab + e6ab e6ab · e7ab + e7ab · e8ab) · $\overline{\textit{adc2ab\_disable}}$	
ghor[c]	g2hab + g3hab + g4hab + g5hab + g6hab + g7hab + (corresponding terms for cd)	any high-level guard discr.
mor[c]	e1ma + e1mb + e2mab + e3mab + e4mab + e5mab + e6mab + e7mab + e8mab + (corresponding terms for cd)	any medium-level center discr.
hor[c]	e1ha + e1hb + e2hab + e3hab + e4hab + e5hab + e6hab + e7hab + e8hab + (corresponding terms for cd)	any high-level center discr.
z1ab	(minrngab + adc2ab) · $\overline{\text{mor}}$ · $\overline{\text{hor}}$ · $\overline{\text{glab}}$	
z2ab	(minrngab + adc2ab) · mor · $\overline{\text{hor}}$ · $\overline{\text{glab}}$	
z > 2ab	minrngab · hor · $\overline{\text{ghor}}$	
[hodo]	$\overline{\textit{hmode0}}$ · $\overline{\textit{hmode1}}$ · (soft0 · soft1) + *hmode0* · $\overline{\textit{hmode1}}$ · (soft0 + soft1) + $\overline{\textit{hmode0}}$ · *hmode1* · soft0 + *hmode0* · *hmode1* · soft1 + *force_hodo*	
trigger	e1a + e1b + e2ab + e3ab + e4ab + e5ab + e6ab + e7ab + e8ab + e9ab + g2ab + g3ab + g4ab + g5ab + g6ab + g7ab + (corresponding terms for cd)	trigger condition
valid	[hodo] · ((z1ab + z1cd) · *hy_enable* + (z2ab + z2cd) · *he_enable* + (z>2ab) + (z>2cd) + (stim · *stim_always_valid*)) · ($\overline{\textit{hazard}}$ + $\overline{\textit{haz\_anti\_en}}$)	coincidence requirement

[a]Inputs are defined in Table IX. Those in italics are commandable, static inputs.
[b]Most terms (other than ghor, mor, hor, [hodo], trigger, and valid) are specific to the AB telescope pair. Corresponding terms exist for the CD telescope pair.
[c]Command bits also exist which allow each term in ghor, mor, and hor to be separately deleted.

TABLE XI
CRIS normal event format

Item	Count	Bits	Sum[a]	Description
Event header				
0	1	8	8	Number of bytes in this event
1	1	1	9	Stimulated event flag
2	1	1	10	Primary telescope pair (AB = 0; CD = 1)
3	1	6	16	Event buffer ID
4	1	1	17	Guard low-level 'OR'
5	1	1	18	Hazard flag
6	1	3	21	# Low-level guards hit ($G1$) in primary telescope pair
7	1	3	24	Range ($R1-2$) in primary telescope pair ($R1$ values: 2–9)
8	1	1	25	Is there 2nd telescope data included in this event?
9	1	1	26	Transmit guard pulse heights in this event?
10	1	1	27	SOFT cluster centroid calculation error encountered
11	1	5	32	Number of SOFT clusters transmitted (N)[b]
12	1	8	40	SOFT # of pixels[c]
13	1	2	42	2nd telescope activity tag bits
14	1	6	48	Instrument cycle counter
2nd telescope event header (present if item 8 is true)				
15	1	2	2	Spare
16	1	3	5	# Low-level guards hit ($G2$) in secondary telescope pair
17	1	3	8	Range ($R2-2$) in secondary telescope pair ($R2$ values: 2–9)
SOFT hodoscope data				
18	N	10	10	SOFT cluster x centroids
19	N	9	19	SOFT cluster y centroids
20	N	5	24	SOFT cluster intensity parameter [c]
Primary telescope data				
Discriminator tag bits				
21	1	16	16	Tag bits: $G7-G2$, $E9-E1A$ ($E1A$ = LSB, $G7$ = MSB)
Center pulse heights				
22	$R1+1$[d]	12	40 to 120	Stack-detector pulse heights + 4 bits 0 pad if $R1$ is even
Guard pulse heights (if item 9 is true)				
23	$G1$	12	12	Guard pulse height
24	$G1$	1	13	Spare
25	$G1$	3	16	Guard address (values: 2–7)
Secondary telescope data (if item 8 is true)				
				Analagous to items 21 through 25, above
Stimulated event parameters (if item 1 is true)				
26	1	4	4	Flags indicating which guard pulsers are active
27	1	4	8	Flags indicating which center pulsers are active
28	1	8	16	guard pulser DAC level
29	1	8	24	center pulser DAC level
30	1	1	25	guard DAC high-gain mode
31	1	1	26	center DAC high-gain mode
32	1	6	32	SOFT LED pulse length

[a]Running total number of bits in each section.
[b]Maximum number of SOFT clusters read out is commandable up to $N_{\max} = 31$.
[c]Encoded as a floating point value.
[d]Both E1 signals always read out.

TABLE XII
CRIS event buffers as assigned at launch

Charge	Range	Number of buffers and rates[a]	Readout priority[b]		
			Good Hodo		Bad Hodo
			HAZ = 0	HAZ = 1	HAZ = 0 or 1
Single-telescope-pair events (one set for A/B, one set for C/D)					
$Z \geq 3$	9 (PEN)	3	34	31	14
$Z \geq 10$	8	3	60	52	26
	5, 6, 7	3	62	54	28
	3, 4	3	61	53	27
	2	3	59	51	22
$3 \leq Z \leq 9$	8	3	56	48	23
	5, 6, 7	3	58	50	25
	3, 4	3	57	49	24
	2	3	55	47	21
$Z = 2$	9 (PEN)	3	33	30	13
	8	3	44	38	18
	5, 6, 7	3	46	40	20
	3, 4	3	45	39	19
	2	3	43	37	17
$Z = 1$	8, 9 (PEN)	3	32	29	12
	3 to 7	3	42	36	16
	2	3	41	35	15
	Total:	51			
Double-telescope-pair events					
$Z \geq 3$	9 (PEN)	1	5	5	5
	4 to 8	1	11	11	11
	2 to 3	1	10	10	10
$Z = 2$	9 (PEN)	1	4	4	4
	4 to 8	1	9	9	9
	2 to 3	1	8	8	8
$Z = 1$	9 (PEN)	1	3	3	3
	4 to 8	1	7	7	7
	2 to 3	1	6	6	6
Stim [c]	9 (typ.)	1	63	63	63
	Total:	10			

[a]Total rates: 51 (A/B single) + 51 (C/D single) + 10 (double) = 112.
Total buffers: 51 (A/B single + C/D single) + 10 (double) = 61.
[b]Higher numbers indicate higher priorities. Buffers 0, 1, and 2 are not used.
[c]Pulser stimulus event.

Following the header(s) are the SOFT hodoscope data. Using the raw SOFT pixel locations and intensities, the on-board microprocessor determines which pixels are adjacent to each other, and calculates the total intensity and the two-dimensional centroid location of each such contiguous cluster of pixels. The resulting position and intensity information occupies three bytes for each cluster.

Silicon-detector pulse-height information follows the SOFT data, starting with the 'primary' telescope pair, that is, the one with the longest range if both telescope pairs were triggered. Tag bits indicating which of the 10 stack and six guard low level discriminators were triggered take up 2 bytes. Stack-detector pulse heights are listed after the tag bits. If guard pulse heights are to be telemetered, they follow the stack detector pulse heights. If data from the second telescope pair are included, they follow the data from the first telescope, in the same sequence (discriminator tag bits, stack pulse heights, guard pulse heights). Finally, if the event is a pulser-stimulated event, it concludes with a four-byte block listing which pulsers were active and the value of their control DAC levels.

Appendix D. CRIS Event Buffers

As discussed in Section 5.4.2, CRIS events are roughly classified onboard based on charge category, range, hazard, and trajectory quality. Events are sorted among 61 buffers according to this classification, and the corresponding rate of events falling in each buffer is counted. Each buffer is assigned a priority which is used in selecting events from the various buffers for readout. Table XII shows the priorities normally assigned to each of the event buffers. The priorities can be changed by command.

Abbreviations: ACE – Advanced Composition Explorer, ACR – anomalous cosmic ray, ADC – analog-to-digital converter, AOG – amplifier/offset gate, ASIC – application-specific integrated circuit, ASCII – American Standard Code for Information Interchange, BPBD – 2-(4-Biphenylyl)-5-(4-tert-butylphenyl)-1,3,4-oxadiazole (scintillation dye), CCD – charge coupled device, CRIS – Cosmic Ray Isotope Spectrometer, CRRES – Combined Release and Radiation Effects Satellite, DAC – digital-to-analog converter, DPOPOP – 1,4-Bis(4-methyl-5-phenyloxazol-2-yl)benzene (scintillation dye), EMA – extramural absorber, FIP – first ionization potential, GCR – galactic cosmic ray, GCRS – galactic cosmic ray source, GSFC – Goddard Space Flight Center, GSI – Gesellschaft für Schwerionenforschung mbH (accelerator laboratory in Darmstadt, Germany), ISEE – International Sun-Earth Explorer, JPL – Jet Propulsion Laboratory, LBNL – Lawrence Berkeley National Laboratory, LED – light emitting diode, LISM – local interstellar medium, MCP – microchannel plate, MLI – multilayer insulation, MSU/NSCL – Michigan State University / National Superconducting Cyclotron Laboratory, NASA – National

Aeronautics and Space Administration, PCB – printed-circuit board, PHA – pulse-height analyzer, RF – radio frequency, r.m.s. – root mean square, SAMPEX – Solar, Anomalous, and Magnetospheric Particle Explorer, S/C – spacecraft, SEP – solar energetic particle, Si(Li) – lithium-drifted silicon detector, SLAM – Structural Loads and Acoustics Measurements (instrument on ACE), SOFT – Scintillating Optical Fiber Trajectory (detector), SW – solar wind, TV – thermal-vacuum, VLSI – very large scale integrated (circuit), ZIF – zero insertion force (connector).

References

Ahlen, S. P.: 1980, 'Theoretical and Experimental Aspects of the Energy Loss of Relativistic Heavily Ionizing Particles', *Rev. Mod. Phys.* **52**, 121–173.

Allbritton, G. A., Andersen, H., Barnes, A., Christian, E. R., Cummings, A. C., Dougherty, B. L., Jensen, L., Lee, J., Leske, R. A., Madden, M. P., Mewaldt, R., Milliken, B., Nahory, B. W., O'Donnell, R., Schmidt, P., Sears, B. R., von Rosenvinge, T. T., Walton, J. T., Wiedenbeck, M. E., and Wong, Y. K.: 1996, 'Large-Diameter Lithium Compensated Silicon Detectors for the NASA Advanced Composition Explorer (ACE) Mission', *IEEE Trans. Nucl. Sci.* **43**, 1505–1509.

Althouse, W. E., Cummings, A. C., Garrard, T. L., Mewaldt, R. A., Stone, E. C., and Vogt, R. E.: 1978, 'A Cosmic Ray Isotope Spectrometer', *IEEE Trans. Geosci. Electronics* **GE-16**, 204–207.

Barnett, R. M. et al.: 1996, 'Review of Particle Properties', *Phys. Rev.* **D54**, 1.

Berezinskiĭ, V. S., Bulanov, S. V., Dogiel, V. A., Ginzburg, V. L., and Ptuskin, V. S.: 1990, *The Astrophysics of Cosmic Rays*, North-Holland, Amsterdam.

Breneman, H. H. and Stone, E. C.: 1985, 'Solar Coronal and Photospheric Abundances from Solar Energetic Particle Measurements', *Astrophys. J.* **199**, L51–L61.

Cassé, M. and Paul, J. A.: 1982, 'On The Stellar Origin of the ^{22}Ne Excess in Cosmic Rays', *Astrophys. J.* **258**, 860–863.

Connell, J. J. and Simpson, J. A.: 1995, 'The *Ulysses* Cosmic Ray Isotope Experiment: Isotopic Abundances of Fe and Ni from High Resolution Measurements', *Proc. 24th Int. Cosmic Ray Conf., Rome* **2**, 602–605.

Connell, J. J. and Simpson, J. A.: 1997a, 'High Resolution Measurements of the Isotopic Composition of Galactic Cosmic Ray C, N, O, Ne, Mg, and Si from the *Ulysses* HET', *Proc. 25th Int. Cosmic Ray Conf., Durban* **3**, 381–384.

Connell, J. J. and Simpson, J. A.: 1997b, '^{26}Al in the Galactic Cosmic Radiation: Measurements with the *Ulysses* HET Instrument', *Proc. 25th Int. Cosmic Ray Conf., Durban* **3**, 393–396.

Cook, W. R., Cummings, A., Kecman, B., Mewaldt, R. A., Aalami, D., Kleinfelder, S. A., and Marshall, J. H.: 1993a, in B. Tsuratani (ed.), 'Custom Analog VLSI for the Advanced Composition Explorer', *Small Instruments Workshop Proc.*, Pasadena, Jet Propulsion Laboratory.

Cook, W. R., Cummings, A. C., Cummings, J. R., Garrard, T. L., Kecman, B., Mewaldt, R. A., Selesnick, R. S., Stone, E. C., and von Rosenvinge, T. T.: 1993b, 'MAST: A Mass Spectrometer Telescope for Studies of the Isotopic Composition of Solar, Anomalous, and Galactic Cosmic Ray Nuclei', *IEEE. Trans. Geosci. Remote Sensing* **31**, 557–564.

Crary, D. J., Binns, W. R., Cummings, A. C., Klarmann, J., Lawrence, D. J., and Mewaldt, R. A.: 1992, 'A Bevalac Calibration of a Scintillating Optical Fiber Hodoscope', *Nucl. Inst. Meth.* **A316**, 311–317.

Davis, A. J., Hink, P. L., Binns, W. R., Epstein, J. W., Connell, J. J., Israel, M. H., Klarmann, J., Vylet, V., Kaplan, D. H., and Ruecroft, S.: 1989, 'Scintillating Optical Fiber Trajectory Detectors', *Nucl. Inst. Meth.* **A276**, 347–358.

Dougherty, B. L., Christian, E. R., Cummings, A. C., Leske, R. A., Mewaldt, R. A., Milliken, B. D., von Rosenvinge, T. T., and Wiedenbeck, M. E.: 1996, in B. A. Ramsey and T. A. Parnell (eds.), 'Characterization of Large-Area Silicon Ionization Detectors for the ACE Mission', *Gamma-Ray and Cosmic-Ray Detectors, Techniques, and Missions*, Proc. SPIE 2806, Society of Photo-Optical Instrumentation Engineers, Denver, pp. 188–198.

DuVernois, M. A. and Thayer, M. R.: 1996, 'The Elemental Composition of the Galactic Cosmic-Ray Source: *Ulysses* High-Energy Telescope Results', *Astrophys. J.* **465**, 982–984.

DuVernois, M. A., Garcia-Muñoz, M., Pyle, K. R., Simpson, J. A., and Thayer, M. R.: 1996, 'The Isotopic Composition of Galactic Cosmic-Ray Elements from Carbon to Silicon: the Combined Release and Radiation Effects Satellite Investigation', *Astrophys. J.* **466**, 457–472.

Ellison, D. C., Drury, L. O'C., and Meyer, J.-P.: 1998, 'Cosmic Rays from Supernova Remnants: A Brief Description of the Shock Acceleration of Gas and Dust', *Space Sci. Rev.* **86**, 203.

Engelmann, J. J., Ferrando, P., Soutoul, A., Goret, P., Juliusson, E., Koch-Miramond, L., Lund, N., Masse, P., Peters, B., Petrou, N., and Rasmussen, I. L.: 1990, 'Charge Composition and Energy Spectra of Cosmic-Ray Nuclei for Elements from Be to Ni. Results from HEAO-3-C2', *Astron. Astrophys.* **233**, 96–111.

Fisher, A. J., Hagen, F. A., Maehl, R. C., Ormes, J. F., and Arens, J. F.: 1976, 'The Isotopic Composition of Cosmic Rays with $5 \leq Z \leq 26$', *Astrophys. J.* **205**, 938–946.

Garcia-Muñoz, M., Mason, G. M., and Simpson, J. A.: 1977, 'The Isotopic Composition of Galactic Cosmic Ray Lithium, Beryllium, and Boron', *Proc. 15th Int. Cosmic Ray Conf., Plovdiv* **1**, 301–306.

Halpern, E. and Marshall, J. H.: 1968, 'A High Resolution Gamma-Ray Spectrometer for Use in Outer Space', *IEEE Trans. Nucl. Sci.* **NS-15**, 242–251.

Halpern, E., Marshall, J. H., and Weeks, D.: 1968, 'A Gamma-Ray Spectrometer for Space Applications', *Nucleonics in Aerospace*, Plenum Press, New York, pp. 98–106.

Harrington, T. M. and Marshall, J. H.: 1968, 'A Pulse-Height Analyzer for Charged Particle Spectroscopy on the Lunar Surface', *Rev. Sci. Instr.* **39**, 184–194.

Harrington, T. M. and Marshall, J. H.: 1969, 'An Electronics System for Gamma-Ray Spectrometry in Space Applications', *IEEE Trans. Nucl. Sci.* **NS-16**, 314–321.

Harrington, T.M., Marshall, J.H., Arnold, J.R., Peterson, L.E., Trombka, J.I., and Metzger, A.E.: 1974, 'The Apollo Gamma-Ray Spectrometer', *Nucl. Instr. Meth.* **118**, 401–411.

Hink, P. L., Binns, W. R., Klarmann, J., and Olevitch, M. A.: 1996, 'The ACE–CRIS Scintillating Optical Fiber Trajectory (SOFT) Detector: A Calibration at the NSCL', in B. A. Ramsey and T. A. Parnell (eds.), *Gamma-Ray and Cosmic-Ray Detectors, Techniques, and Missions*, Proc. SPIE 2806, Society of Photo-Optical Instrumentation Engineers, Denver, pp. 199–208.

Hubert, F., Bimbot, R., and Gauvin, H.: 1990, 'Range and Stopping-Power Tables for 2.5–500 MeV/Nucleon Heavy Ions In Solids', *Atom. Dat. Nucl. Dat. Tables* **46**, 1–213.

Leske, R. A.: 1993, 'The Elemental and Isotopic Composition of Galactic Cosmic-Ray Nuclei from Scandium through Nickel', *Astrophys. J.* **405**, 567–583.

Leske, R. A. and Wiedenbeck, M. E.: 1993, 'Composition Measurements from ISEE-3: Fluorine through Calcium', *Proc. 23rd Int. Cosmic Ray Conf., Calgary* **1**, 571–574.

Letaw, J. R., Adams, J. H., Silberberg, R., and Tsao, C. H.: 1985, 'Electron-Capture Decay of Cosmic Rays', *Astrophys. Space Sci.* **114**, 365–379.

Letaw, J. R., Silberberg, R., and Tsao, C. H.: 1993, 'Comparison of Distributed Reacceleration and Leaky-Box Models of Cosmic-Ray Abundances ($3 \leq Z \leq 28$)', *Astrophys. J.* **414**, 601–611.

Lukasiak, A., McDonald, F. B., and Webber, W. R.: 1997, 'Study of Elemental and Isotopic Composition of Cosmic Ray Nuclei Ca, Ti, V, Cr, Mn and Fe', *Proc. 25th Int. Cosmic Ray Conf., Durban* **3**, 357–360.

Lund, N.: 1989, in C. J. Waddington (ed.), 'The Abundances in the Cosmic Radiation (The Elements Lighter than Ge)', *Proceedings of the Symposium on Cosmic Abundances of Matter*, AIP Conf. Proc. 183, American Institute of Physics Press, Minneapolis, pp. 111–123.

Mewaldt, R. A.: 1989, in C. J. Waddington (ed.), 'The Abundances of Isotopes in the Cosmic Radiation', *Proceedings of the Symposium on Cosmic Abundances of Matter*, AIP Conf. Proc. 183, American Institute of Physics Press, Minneapolis, pp. 124–146.

Meyer, J.-P.: 1985, 'Solar-Stellar Outer Atmospheres and Energetic Particles, and Galactic Cosmic Rays', *Astrophys. J. Suppl.* **57**, 173–204.

Meyer, J.-P., Drury, L. O'C., and Ellison, D. C.: 1998, 'A Cosmic Ray Composition Controlled by Volatility and A/Q Ratio. SNR Shock Acceleration of Gas and Dust', *Space Sci. Rev.* **86**, 179.

Payne, M. G.: 1969, 'Energy Straggling of Heavy Charged Particles in Thick Absorbers', *Phys. Rev.* **185**, 611–623.

Ptuskin, V. and Soutoul, A.: 1998, 'Cosmic Ray Clocks', *Space Sci. Rev.* **86**, 225.

Rossi, B.: 1952, *High-Energy Particles*, Prentice-Hall, Englewood Cliffs, p. 31.

Soutoul, A., Cassé, M., and Juliusson, E.: 1978, 'Time Delay Between the Nucleosynthesis of Cosmic Rays and Their Acceleration to Relativistic Energies', *Astrophys. J.* **219**, 753–755.

Stone, E. C.: 1989, in C. J. Waddington (ed.), 'Solar Abundances as Derived from Solar Energetic Particles', *Proceedings of the Symposium on Cosmic Abundances of Matter*, AIP Conf. Proc. 183, American Institute of Physics Press, Minneapolis, pp. 72–90.

Stone, E. C. and Wiedenbeck, M. E.: 1979, 'A Secondary Tracer Approach to the Derivation of Galactic Cosmic Ray Source Isotopic Abundances', *Astrophys. J.* **231**, 606–623.

Stone, E. C., Cohen, C. M. S., Cook, W. R., Cummings, A. C., Gauld, B., Kecman, B., Leske, R. A., Mewaldt, R. A., Thayer, M. R., Dougherty, B. L., Grumm, R. L., Milliken, B. D., Radocinski, R. G., Wiedenbeck, M. E., Christian, E. R., Shuman, S., von Rosenvinge, T. T.: 1998: 'The Solar Isotope Spectrometer for the Advanced Composition Explorer', *Space Sci. Rev.* **86**, 357.

Thayer, M. R.: 1997, 'An Investigation into Sulfur Isotopes in the Galactic Cosmic Rays', *Astrophys. J.* **482**, 792–795.

Webber, W. R., Lukasiak, A., McDonald, F. B., and Ferrando, P.: 1996, 'New High-Statistical-High-Resolution Measurements of the Cosmic-Ray CNO Isotopes from a 17-Year Study Using the Voyager 1 and 2 Spacecraft', *Astrophys. J.* **457**, 435–439.

Webber, W.R., Lukasiak, A., and McDonald, F. B.: 1997, 'Voyager Measurements of the Mass Composition of Cosmic-Ray Ne, Mg, Si, and S Isotopes', *Astrophys. J.* **476**, 766–770.

Wiedenbeck, M. E. and Greiner, D. E.: 1980, 'A Cosmic-Ray Age Based on the Abundance of ^{10}Be', *Astrophys. J.* **239**, L139–L142.

Zaerpoor, K., Chan, Y. D., DiGregorio, D. E., Dragowsky, M. R., Hindi, M. M., Isaac, M. C. P., Krane, K. S., Larimer, R. M., Macciavelli, A. O., Macleod, R. W., Miocinovic, P., and Norman, E. B.: 1997, 'Galactic Confinement Time of Iron-Group Cosmic Rays Derived from the ^{54}Mn Chronometer', *Phys. Rev. Letters* **79**, 4306–4309.